Sparse Array for Wireless Sensor Networks and Wireless Communications

by

HAO LIANG

Presented to the Faculty of the Graduate School of

The University of Texas at Arlington in Partial Fulfillment

of the Requirements

for the Degree of

DOCTOR OF PHILOSOPHY

THE UNIVERSITY OF TEXAS AT ARLINGTON

May 2017

ACKNOWLEDGEMENTS

First of all, I would like to thank my advisor, Dr. Qilian Liang, for all his guidance and encouragement. I have a wonderful experience in my years as a Ph.D. student largely because of him. He has made himself available over all these years whenever I want to have a discussion. I want to thank him for all the wise advices he has given to me on research, career and life. His enthusiasm and his taste in research problems have deeply influenced me and helped me to develop as a better researcher.

I also want to thank the faculty members in Electrical Engineering at UTA for the friendly, collaborative and stimulating atmosphere they have created for the department. In particular, I want to express my gratitude to Dr. Yan Wan, Dr. Jean Gao, Dr. Dillion, Dr. Manry for serving on my comprehensive exam committee.

Moreover, I also want to thank all my colleagues and visiting scholars in the Wireless Communication Lab: Xin Wang, Junjie Chen, Zhuo Li, Ishrat Maherin, Shitong Yuan, Na Wu, Longwei Wang, Ganlin Zhao, Dr. Baoju Zhang, Dr. Weixia Zou and Dr. Jiasong Mu. Thanks for all the things they taught me!

I am grateful to all the teachers who taught me during the years I spent in school, first in Tianjin, then in Cleveland and finally in the UTA.

Last but not least, I am sincerely grateful to my parents and wife. I want to thank them the most for always being supportive for all my choices, and offering wise

advices and selfless helps through my toughest time. I have no way to thank them for their priceless love, care, inspiration, patience, and encouragement, but to dedicate this thesis to them.

<div align="right">January, 2017</div>

ABSTRACT

Sparse Array for Wireless Sensor Networks and Wireless Communications

HAO LIANG, Ph.D.

The University of Texas at Arlington, 2017

Supervising Professor: Qilian Liang

Underwater target detection and recognition has been widely used nowadays. In this dissertation, we show that the 3-D nested-array system can provide $O(N^2)$ degree of freedom by using only N physical sensors when the second order statistics of the received data is used, which means we can use less sensors to get a better performance. We propose a maximum likelihood (ML) estimation algorithm for underwater target size detection. Theoretical analysis illustrates that our underwater sensor network can tremendously reduce the variance of target estimation. We show that our ML estimator is unbiased and the variance of parameter estimation matches the Cramer-Rao lower bound.We also propose a maximum likelihood automatic target recognition (ML-ATR) algorithm for nonfluctuating as well as fluctuating targets. Theoretical analysis illustrates that our underwater ML-ATR method can tremendously reduce the number of physical sensors while maintain in a good performance

Moreover, a novel deployment for multi-cell cooperative cellular network based on the two-dimensional (2D) coprime array, and analysis on its sum rate capac- ity are proposed. Taking advantage of that the 2D coprime-array system can provide $O(N^2)$

degree of freedom by using only N physical sensors when the second order statistics of the received data is used, we show that the derivation procedure of average sum-rate capacity for the cooperative cellular network is still valid for the coprimed distributed base stations (BSs) in the non-fading and Rayleigh fading channels.

We also study sense-through-foliage target detection using ultra-wideband (UWB) radars. We propose a Discrete-Cosine-Transform (DCT)-based approach for sense-through- foliage target detection when the echo signal quality is good, and a Radar Sensor Network (RSN) and DCT-based approach when the echo signal quality is poor. A RAKE structure which can combine the echos from different cluster-members is proposed for clusterhead in the RSN. We compared our approach with the ideal case when both echos are available, i.e., echos with target and without target. We also compared our approach against the scheme in which 2- D image was created via adding voltages with the appropriate time offset as well as the matched filter-based approach. We observed that the matched filter-based couldnot work well because the UWB channel has memory.

In the last Chapter, we propose a transfer entropy based approach for sense-through-foliage target detection. It is the first time to apply Transfer Entropy(TE) to real world target detection. Two different types of data are provided by Air Force Office of Scientific Research in terms of radar echo signal quality. We compare our approach with the case of linear regression approach for target detection. Simulation results show that our scheme works better than the existing approaches.

TABLE OF CONTENTS

LIST OF ILLUSTRATIONS

LIST OF TABLES

CHAPTER 1

INTRODUCTION

Underwater target detection plays an important role in military, ocean exploitation and disaster rescue and prediction. The authors in [51][52] proposed two new sparse array deploy method, namely co-prime array and nested array. This method can dramatically increase the degree of freedom compared to the actual number of physical sensors. 2-D nested array and its application were presented in [53][54]. Smith form decomposition of the integer matrix is used in the design of the 2-D nested array. They demonstrated that the number of source can be much larger than the number of physical sensors. In Chapter 1, singular value decomposition is use so that the matrix value is not restricted to have integer anymore. The minimum redundancy array was introduced in [55], which can have a smaller number of redundancy sensors in the array. As underwater environment is broad and deep, the 2-D case is not applicable for this situation. We extend it into 3D case.

With the forthcoming 500 million connections and explosion of mobile broadband data, heterogeneous networks with a combined approach including improving, densifying and finding better deployment of the cells are becoming the future way to enhance network capacity and performance [42].

Several studies have addressed the cell planning and interference issues in the past. In [43], different symmetric cell deployment strategies have been studied based on inter-site distance and it is concluded that the network capacity can be enhanced

through denser deployment of cells. In [44] the authors propose to deploy a massive amount of small cells in order to increase the total capacity and reduce the energy consumption.

However, when the cells are deployed in a super dense way, the inter-cell interference problem would become dominant. In a high interference scenario with many line-of-sight (LOS) interferers around, keep adding cells regardless of the surrounding environment will not always help to improve the network performance.[45]

Hence, finding better deployment of BSs and increasing the level of collaboration would be a better way to achieve higher capacity. In Chapter 3, a novel coprime distributed network is proposed which can increasing the degree of freedom of the co-arrays to reduce the number of physical sensor while maintaining the same performance. In [46], another sparse deployment method named nested-array was introduced.

UWB radars are used nowadays for different applications such as subsurface sensing, classification of aircrafts, collision avoidance, etc. In all of these applications the ultra-high resolution of UWB radars is essentially used [62]. UWB radar emissions are at a relatively low frequency-typically between 100 MHz and 3 GHz. Additionally, the fractional bandwidth of the signal is very large (greater than 0.25). In this definition, bandwidth means the difference between the highest and lowest frequencies of interest and contains about 95% of the signal power [39][40]. Such radar sensor has exceptional range resolution that also has an ability to penetrate many common materials (e.g., walls). Law enforcement personnel have used UWB ground penetrating radars (GPRs) for at least a decade.In chapter 4, we will study

sense-through-foliage target detection using UWB radars.

Chapter 2 implements the 3D nested-array theory into underwater target detection and recognition. In Chapter 3, a novel deployment for multi-cell cooperative cellular network based on the two-dimensional (2D) coprime array, and analysis on its sum rate capac- ity are proposed. Sense-through-foliage target detection using ultra-wideband (UWB) radars is studied in Chapter 4. An information theory based Sense-through-foliage target detection using Transfer Entropy is proposed in Chapter 5.

CHAPTER 2

Target Detection and Recognition Based on 3-D Sparse Underwater Sonar Array

Network

2.1 Introduction

In the case of our proposed nested array , we shall demonstrate that using only the second order statistics of the source, it is possible to get the effect of a 3D array of O(MN) "virtual "sensors using only M + N physical sensors. We want these virtual sensors to completely filling up a parallelepiped (FPD) with no missing sensor.

The relationship between distance and size in underwater situation was studied in [56]. In [94], algorithm to extract the target size information from a sequence of 2D acoustic images acquired by a forward looking sonar has been proposed. In [57], ML algorithm for underwater target detection is proposed. The Cramer-Rao bound of the MUSIC estimation is provided in [58].

Underwater target size recognition is very similar to radar cross section [95] since it is proportional to received signal power. In Chapter 2, we assume that the distance between the target and sensor is know, since it can be easily calculate base on the time duration between the sent signal and its received echo.

The rest of this chapter is organized as follows. In Section 2, we give a brief introduction of sparse arrays system. In Section 3, we develop a maximum-likelihood estimation algorithm for target size parameter estimation using underwater sensor ar-

ray network. In Section 4, Monte Carlo simulation result is provided. The conclusion is drew in Section 5.

2.2   3-D NESTED ARRAY SENSOR NETWORK MODEL

1. Definition of Multidimensional lattices and matrix We shall first review several concept about multidimensional lattices [59]. Given a $D \times D$ singular matrix V, the D dimensional lattice generated by this matrix is defined as

$$LAT(V) = \{t : t = V_n\} \qquad (2.1)$$

Where $n \in N^{D \times 1}$ is an integer vector. The matrix V is called the generator of that lattice. An important concept related to LAT(V) is that of the fundamental parallelepiped (FPD). The FPD of $V \in C^{D \times D}$ in D dimensions is defined as the set of all vectors of the form

$$\{V_x, x \in [0 \quad 1)^D\} \qquad (2.2)$$

Fig. 1 demonstrates the FPD in three dimension case.

Suppose M is a $m \times n$ matrix whose entries come from the field K, which is either the field of real numbers or the field of complex numbers. Then there exists a factorization of the form

$$M = U\Sigma V^* \qquad (2.3)$$

where U is a $m \times m$ unitary matrix over K(orthogonal matrix if $K = R$),Σ is a $m \times m$ diagonal matrix with non-negative real numbers on the diagonal, and the $n \times n$ unitary matrix, V^* denotes the conjugate transpose of the $n \times n$ unitary matrix V.

Such a factorization is called a singular value decomposition of M. The diagonal

5
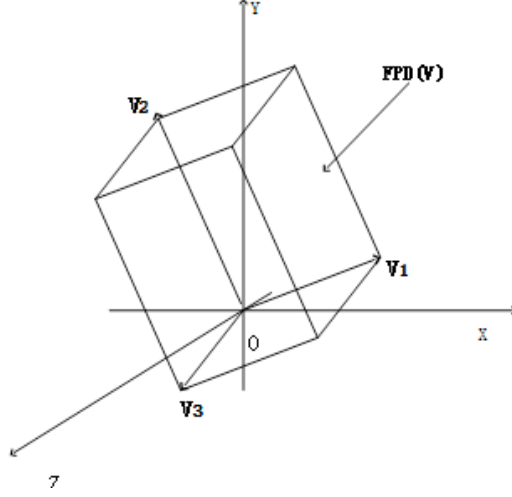
Figure 2.1. FPD of the lattice generated by the generator matrix $V = [v_1 v_2 v_3]$..

entries σ_i of Σ are known as the singular values of M. A common convention is to list the singular values in descending order. In this case, the diagonal matrix Σ is uniquely determined by M.

Definition: Contiguous Sensors on a Lattice): In three dimensions , a collection of sensors on LAT(V) is said to be contiguous (also referred to as "array without holes," or "array with no missing sensors") if the sensor location are given by $\{V[v_1 \quad v_2 \quad v_3]^T, N_{11} \leq v_1 \leq N_{13}, N_{21} \leq v_2 \leq N_{23}, N_{31} \leq v_3 \leq N_{33}\}$. Where N_{xy} are some real numbers.

2. Nested Array on Lattices Consider two lattices with 3×3 generator matrices $N^{(S)}$ and $N^{(D)}$ satisfying,

$$N^{(S)} = N^{(D)} P \tag{2.4}$$

Where P is a 3×3 matrix.

$$N_1^{(S)} + N_2^{(S)} + N_3^{(S)} = N^{(S)} \tag{2.5}$$

$$Det|P| = |N^{(D)}| \tag{2.6}$$

6

Lemma 1: The cross difference co-array between $LAT(N^{(S)})$ and $LAT(N^{(D)})$ has all sensors located on the dense lattice generated by $N^{(D)}$.

Proof: The cross difference co-array between $LAT(N^{(S)})$ and $LAT(N^{(D)})$ has sensors located at $N^{(S)}n^{(S)} - N^{(d)}n^{(d)}$. Since $N^{(S)} = N^{(D)}P$, the differences can be written as $N^{(D)}(Pn^{(S)} - n^{(d)}) = N^{(D)}n$. Hence, the cross difference co-array has its sensors on the dense lattice $N^{(D)}$.

3. Properties of Nested Array We first define

$$SFPD(N^{(S)}), k_1, k_2, k_3) = \{N^{(S)}([k_1, k_2, k_3]^T - x), x \in [0, 1)^2\} \qquad (2.7)$$

hence k_1, k_2, k_3 can be arbitrary real numbers and SFPD stands for "shifted FPD", where $FPD(N^{(S)})$ is shift by the vector $[k_1, k_2, k_3]^T$. Theorem 1: Consider $N^{(S)}$ and $N^{(D)}$ related by matrix P as $N^{(S)} = N^{(D)}P$.

Then

1) Any point $N^{(d)}n$ on $LAT(N^{(d)})$ can be expressed as $N^{(D)}n = N^{(S)}n^{(S)}) - N^{(D)}n^{(D)}$ where $n^{(S)}$ is a real vector and $n^{(D)}$ FPD(P).

2) All points on $LAT(N^{(d)})$ contained within $SFPD(N^{(S)}, k_1, k_2, k_3)$ can be generated by the differences $\{N^{(S)}([k_1, k_2, k_3]^T - N^{(D)}n^{(D)}, n^{(D)} \in FPD(P)\}$.

Proof:

Any point $N^{(D)}n$ on $LAT(N^{(D)})$ is also in $SFPD(N^{(S)}, k_1, k_2, k_3)$ if and only if

$$SFPD(N^{(S)}, k_1, k_2, k_3) = \{N^{(S)}([k_1, k_2, k_3]^T - x), x \in [0, 1)^2\}$$

This is the same as n $= P[k_1, k_2, k_3]^T - n^{(d)}$. This holds when $N^{(D)}n$ belongs to $SFPD(N^{(S)}, k_1, k_2, k_3)$. Hence all elements on $LAT(N^{(D)})$ inside $SFPD(N^{(S)}, k_1, k_2, k_3)$ can be generated by the set of differences $\{N^{(S)}([k_1, k_2, k_3]^T - N^{(D)}n^{(D)}, n^{(D)} \in FPD(P)\}$. Hence we get a higher DOF. An Example: Fig .2 shows a 2 level

7
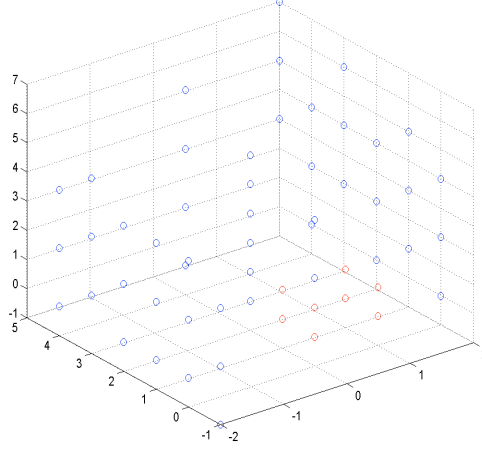
Figure 2.2. 3D nested array.

nested array with randomly generated $N^{(D)}$ and P=$\begin{pmatrix} 2 & 0 & 0 \\ 1 & 2 & 0 \\ 1 & 1 & 2 \end{pmatrix}$ hence the

dense array has $Det|P| = N^{(D)} = 8$ sensors. We assume $N^{(S)} = 48$, therefore

the sparse array has 48 sensors located on $LAT(N^{(S)} = N^{(D)}P)$. The different

co-array elements are shown in Fig.3. There are $8 \times 48 = 384$ virtual sensors

filling up the 48 shifted FPDs of the sparse lattice.

2.3   Maximum Likelihood Algorithm For Target Size Estimation

For underwater sensor array network, the signal from different sensor will inter-

ference each other . We choose the waveform for sensor i as

$$x_i(t) = \sqrt{\frac{1}{T}} exp[j2\pi(\beta + \delta_i)t] \tag{2.8}$$

Which means there is a frequency shift $\delta - i$ for sensor i. To minimize the

interference from one sensor to another, the value for $\delta - i$ should be chosen as

8
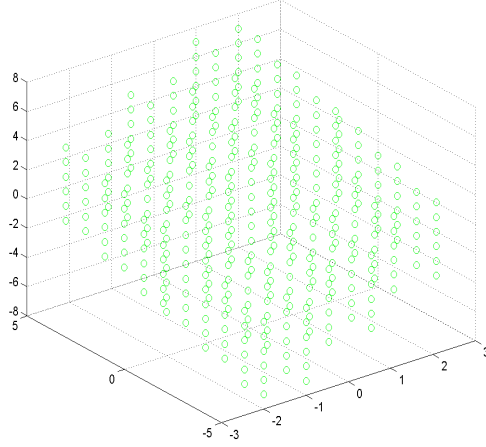
Figure 2.3. Corresponding difference co-array.

$\delta - i = \frac{i}{T}$, so that the waveform will be orthogonal to each other.

In this chapter, we assume the target is nonfluctuating target with size S, and the target reflected signal strength is γ, so γ^2 is proportional to size S, and we assume the S will be known if γ^2 can be estimated. According to the channel model in [57], the I and Q subchannels of $a_{kl}(u)$ follows zero-mean Gaussian distribution. Let

$$A_{kl}(u) = a_{kl}^I(u) + j a_{kl}^Q(u) \tag{2.9}$$

Then the reflected signal from sensor m is

$$Z_m(u) \approx \gamma \sum_l \sum_k a_{kl}(u) + n(u) \tag{2.10}$$

$n(u) = n_I(u) + j n_Q(u)$ follows zero-mean complex Gaussian distribution with variance σ^2 for I and Q subchannels, and

$$E\{\sum_l \sum_k |a_{kl}(u)|^2\} = 1 \tag{2.11}$$

Since $a_{kl}(u)$ and n(u) are zero-mean complex Gaussian random variables, so $\gamma \sum_l \sum_k a_{kl}(u) + n(u)$ is a zero-mean Gaussian variable with variance

9

$\gamma^2 E\{\sum_l \sum_k |a_{kl}(u)|^2/2\}+\sigma^2=\gamma^2/2+\sigma^2$, which means that $y_m = |Z_m(u)|$ follows Rayleigh distribution with parameter $\sqrt{\gamma^2/2+\sigma^2}$

$$f(y_m) = \frac{y_m}{\gamma^2/2+\sigma^2} exp[-\frac{y_m}{2(\gamma^2/2+\sigma^2)})] \tag{2.12}$$

The mean value of y_m is $\sqrt{\frac{\pi(\gamma^2/2+\sigma^2)}{2}})$ and the variance is $\frac{(4-\pi)(\gamma^2/2+\sigma^2)}{2}$. The variance of signal is $\frac{(4-\pi)\gamma^2}{4}$ and the variance of the noise is $\frac{(4-\pi)\sigma^2}{2}$.

The PDF of y is

$$f(y) = \prod_{m=1}^{M} f(y_m) \tag{2.13}$$

So the ML algorithm is to estimate the target size value $\gamma^2/2$,

Let

$$\theta = \gamma^2/2 \tag{2.14}$$

Then

$$\hat{\theta}_{ML}(y) = arg \sup_{\theta \in R^+} f(y) \tag{2.15}$$

The value of target size S will be got when is estimated. Taking both side by natural logarithm,

$$logf(y) = \sum_{m=1}^{M} [log(\frac{y_m}{\theta+\sigma^2}) - \frac{y_m^2}{2(\theta+\sigma^2)}] \tag{2.16}$$

Since it is a continuous function for $y_m > 0$ and $\theta > 0$, so a necessary condition for ML estimation is

$$\frac{\partial}{\partial\theta}logf(y)|_{\theta=\hat{\theta}_{ML(y)}} = \frac{\sum_{m=1}^{M} y_m^2 - 2M(\theta+\sigma^2)}{2(\theta+\sigma^2)^2} = 0 \tag{2.17}$$

Which has the unique solution

$$\hat{\theta}_{ML}(y) = \frac{\sum_{m=1}^{M} y_M^2}{2M} - \sigma^2 \tag{2.18}$$

Considering $\theta \geq 0$,

$$\hat{\theta}_{ML}(y) = max[\frac{\sum_{m=1}^{M} y_M^2}{2M} - \sigma^2, 0] \tag{2.19}$$

Since

$$\frac{\partial^2}{\partial\theta^2}\log f(y)|_{\theta=\hat{\theta}_{ML(y)}} = -\frac{4M^3}{(\sum_{m=1}^{M} y_m^2)^2} < 0 \tag{2.20}$$

The expectation of $\hat{\theta}_{ML(y)}$ is

$$E_\theta[\hat{\theta}_{ML(y)}] = \int_0^\infty \frac{\sum_{m=1}^{M} y_m^2}{2M} f(y_m) dy_m - \sigma^2 \tag{2.21}$$

$$= \int_0^\infty \frac{\sum_{m=1}^{M} y_m^2}{2M} \frac{y_m}{\theta+\sigma^2} exp[-\frac{y_m^2}{2(\theta+\sigma^2)}] dy_m - \sigma^2 = \theta \tag{2.22}$$

So it is an unbiased estimator. Fisher's information would be

$$I_\theta = -E_\theta[\frac{\partial^2}{\partial\theta^2}\log f(y)] = -E_\theta[\frac{M(\theta+\sigma^2) - \sum_{m=1}^{M} y_m^2}{(\theta+\sigma^2)^3}] \tag{2.23}$$

As y_m with the mean value of $\sqrt{\frac{\pi(\theta+\sigma^2)}{2}}$ and variance $\frac{(4-\pi)(\theta+\sigma^2)}{2}$, so the CRLB is

$$Var_\theta[\hat{\theta}(y)] \geq \frac{1}{I_\theta} = \frac{(\theta+\sigma^2)^2}{M} \tag{2.24}$$

We can get to the conclusion that $\hat{\theta}_{ML}(y)$ can achieve the CRLB theoretically and the CRLB is inverse proportionally to the number of sensors M in underwater sensor array network. That means the performance of our estimation gets better with larger M value.

2.3.1 Simulation

We ran 106 realization simulation using Monte Carlo method at each SNR value, and we applied the ML estimation algorithm to estimate the $\hat{\theta}$. In Fig. 4 and Fig. 5, we plotted the variance of the target size ML estimator with 56 physical sensor versus 384 virtual sensors.

From the figure, we find that 1) The curve of actual variance of the estimator is almost overlapping the CRLB curve. Our estimator is an unbiased estimator and the variance of parameter estimator matches CRLB. 2) The variance reduce
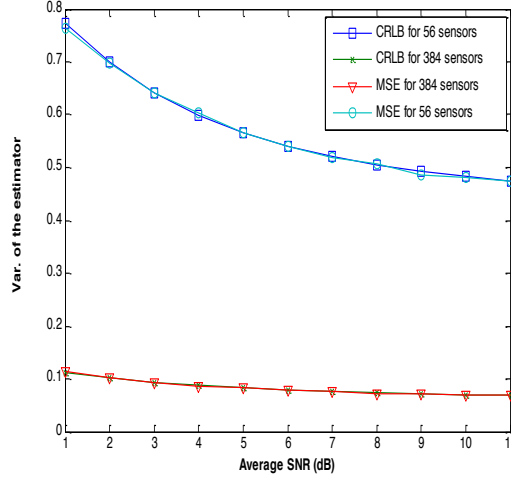
Figure 2.4. Variance of the Estimator with different number of sonars, $\theta = 1$.

when we increase the number of sensors, and they have a reverse proportional relationship.

2.3.2 Conclusion

In this chapter, we extend the the nested-array algorithm into 3-D underwater case which is a combination of O(M+N) sensors distributed over nonseparable lattices, whose difference co-array can give rise to a much larger 3D array with O(MN) sensors on the dense lattice.

Based on the nested-array model, we proposed a ML estimation algorithm for the underwater nested array senor network, with M+N physical sensors we can achieve the performance of $M \times N$ virtual sensors. This method can tremendously reduce the variance of parameter estimation. Simulations further validate these results.

12
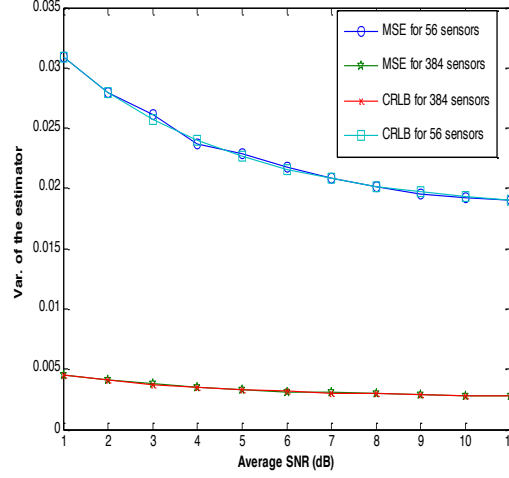
Figure 2.5. Variance of the Estimator with different number of sonars , $\theta = 5$.

2.4   MAXIMUM-LIKELIHOOD AUTOMATIC TARGET RECOGNITION

We use the same waveform we designed in section 2.3.

2.4.1   SSN with two sonar sensors

Assume there are two sonar sensors i and n, the ambiguity function(AF) of sonar i will be

$$A_i(t_i, t_n, F_{Di}, F_{Dn}) = |\int_{-\infty}^{\infty} [x_i(t)exp(j2\pi F_{Di}t) + x_n(t-t_n) \times exp(j2\pi F_{Dn}t)x_i^*(t-t_i)dt|$$

$$(2.25)$$

$$\leqslant |\int_{-T/2+max(t_i,t_n)}^{T/2+min(t_i,t_n)} x_n(t-t_n)exp(j2\pi F_{Dn}t)x_i^*(t-t_i)| + |\int_{-T/2+t_i}^{T/2} x_i(t)exp(j2\pi F_{Di}t)x_i^*(t-t_i)dt|$$

$$(2.26)$$

$$= |\int_{-T/2+max(t_i,t_n)}^{T/2+min(t_i,t_n)} x_n(t-t_n)exp(j2\pi F_{Dn}t)x_i^*(t-t_i)| + |\frac{Esin[\pi F_{Di}(T-|t_i|)]}{T\pi F_{Di}}| \quad (2.27)$$

In this chapter, we assume that the sonar sensors are synchronized that $t_i = t_n = \tau$ to make the problem easier. Hence,

$$A_i(\tau, F_{Di}, F_{Dn}) \approx |Esinc[\pi(n-i+F_{Dn}T)]| + |\frac{Esin[\pi F_{Di}(T-|\tau|)]}{T\pi F_{Di}}| \qquad (2.28)$$

13

And we will have 3 special cases:

- If $F_{Di} = F_{Dn} = 0$,

$$A_i(\tau, 0, 0) \approx |\frac{E(T - |\tau|)}{T}| \qquad (2.29)$$

- If $\tau = 0$,

$$A_i(0, F_{Di}, F_{Dn}) \approx |Esinc[\pi(n - i + F_{Dn}T)]| + |\frac{Esin[\pi F_{Di}T]}{T\pi F_{Di}}| \qquad (2.30)$$

- If $F_{Di} = F_{Dn} = 0, \tau = 0$

$$A_i(0, 0, 0) \approx E \qquad (2.31)$$

2.4.2   SSN with multiple sonar sensors

The problem can be extended into multiple sensor case. Make the time delay τ for each sonar to be the same. The AF for sonar 1 will be,

$$A_1(\tau, F_{D_1}, ..., F_{D_M}) \approx \sum_{i=2}^{M} |Esinc[\pi(i - 1 + F_{D_1}T)]| + |\frac{Esin[\pi F_{D_1}(T - |\tau|)]}{T\pi F_{D_1}}| \qquad (2.32)$$

Similarly, we have the following 3 special cases:

- If $F_{D_1} = F_{D_2} = ... = F_{D_M} = 0$,

$$A_1(\tau, 0, 0, ..., 0) \approx |\frac{E(T - |\tau|)}{T}| \qquad (2.33)$$

- If $\tau = 0$,

$$A_1(0, F_{D_1}, F_{D_2}, ..., F_{D_M}) \approx |Esinc[\pi(n - i + F_{D_1}T)]| + |\frac{Esin[\pi F_{D_1}T]}{T\pi F_{D_1}}| \qquad (2.34)$$

- If $F_{D_1} = F_{D_2} = ... = F_{D_M} = 0, \tau = 0$

$$A_1(0, 0, ..., 0) \approx E \qquad (2.35)$$

2.4.3 MAXIMUM-LIKELIHOOD AUTOMATIC TARGET RECOGNITION

In SSN, each sonar can provide its waveform parameter to its clusterhead sonar, and the clusterhead sonar can combine the waveform from its cluster members. Received signal for clusterhead sonar 1 is,

$$r_1(u,t) = \sum_{i=1}^{M} \alpha(u)x_i(t-t_i)exp(j2\pi F_{D_i}t) + n(u,t) \tag{2.36}$$

which can be regards as a constants for nonfluctuating targets and Swerling target model for fluctuating targets. A RAKE structure is used to combine the received signal.

$$Z_1(u; t_1..., t_M, F_{D_1}, ..., F_{D_M}) = \int_{-T/2}^{T/2} r_1(u,t)x_1^*(t-t_1)dt \tag{2.37}$$

$$= \int_{-T/2}^{T/2} [\sum_{i=1}^{M} \alpha(u)x_i(t-t_i)exp(j2\pi F_{D_i}t) + n(u,t)]x_1^*(t-t_1)dt \tag{2.38}$$

Assuming $t_1 = t_2 = ... = t_M = \tau$, then,

$$Z_1(u; \tau, F_{D_1}, ..., F_{D_M}) \approx \sum_{i=2}^{M} \alpha(u)Esinc[\pi(i-1+F_{D_i}T)] + \frac{\alpha(u)Esin[\pi F_{D_1}(T-|\tau|)]}{T\pi F_{D_1}} + n(u,t) \tag{2.39}$$

Therefore $Z_m(u; \tau, F_{D_1}, ..., F_{D_M})$ consists of three parts, namely signal, interference, noise. There is also three special cases for $Z_m(u; \tau, F_{D_1}, ..., F_{D_M})$,

- When $F_{D_1} = F_{D_2} = ... = F_{D_M} = 0$,

$$Z_m(u; \tau, 0, 0, ..., 0) \approx \frac{E\alpha(u)(T-|\tau|)}{T} + n(u,t) \tag{2.40}$$

- If $\tau = 0$,

$$Z_m(u; \tau, F_{D_1}, ..., F_{D_M}) \approx \sum_{i=1, i\neq M}^{M} \alpha(u)Esinc[\pi(i-m+F_{D_i}T)] + \frac{\alpha(u)Esin[\pi F_{D_m}T]}{T\pi F_{D_1}} + n(u) \tag{2.41}$$

- If $F_{D_1} = F_{D_2} = ... = F_{D_M} = 0 and \tau = 0$,

$$Z_m(u; 0, 0, 0, ..., 0) \approx E\alpha(u) + n(u) \tag{2.42}$$

15

2.4.4 ML-CATR For Non-fluctuating Targets

For nonfluctuating targets, the SCS $\alpha_m(u)$ is just a constant α for a given target. In Equation 2.38, $n(u, \tau)$ is a zero-mean Gaussian random variable for a given τ, so $|Z_m(u, 0, 0, 0, ..., 0)|$ follows a Rician distribution, Let $y_m \triangleq |Z_m(u, 0, 0, 0, ..., 0)|$; then the pdf of y_m is

$$f(y_m) = \frac{2y_m}{\sigma^2} exp[-\frac{y^2 + \lambda^2}{\sigma^2}] I_0(\frac{2\lambda y_m}{\sigma^2}) \tag{2.43}$$

Where

$$\lambda = E\alpha \tag{2.44}$$

σ^2 is the noise power (with I and Q subchannel power $\sigma^2/2$), and I_0 is the zero-order modified Bessel function of the first kind. Let $y \triangleq [y_1, y_2, ..., y_m]$, then the pdf of y is,

$$f(y) = \prod_{m=1}^{M} f(y_m) \tag{2.45}$$

Therefore the ML-CATR algorithm to decide a target category C can be expressed as,

$$\begin{aligned} C &= arg \max_{n=1}^{N} f(y|\lambda = E\alpha_n) \\ &= arg \max_{n=1}^{N} \prod_{m=1}^{M} \frac{2y_m}{\sigma^2} exp[-\frac{y_m^2 + E^2\alpha_n^2}{\sigma^2}] I_0(\frac{2E\alpha_n y_m}{\sigma^2}) \end{aligned} \tag{2.46}$$

2.4.5 ML-CATR For fluctuating Targets

It is more practical to use Fluctuating target modeling when it comes to the underwater case and the target SCS is drawn from either Rayleigh or chi-square pdf. In this work we are using the "Swerling 2" model, which is a Rayleigh distribution with pulse-to-pulse decorrelation and its I and Q subchannels follow zero-mean Gaussian distributions with a variance γ^2. Assume,

$$\alpha(u) = \alpha_I(u) + j\alpha_Q(u) \tag{2.47}$$

And n(u) follows a zero-mean complex Gaussian distribution with a variance σ^2 for the I and Q subchannels. Therefore $y_m \triangleq |Z_m(u; 0, 0, 0, ..., 0)|$ follows a Rayleigh distribution with a parameter, $\sqrt{E^2\gamma^2 + \sigma^2}$

$$f(y_m) = \frac{y_m}{E^2\gamma^2 + \sigma^2} exp(-\frac{y_m^2}{E^2\gamma^2 + \sigma^2}) \tag{2.48}$$

Let $y \triangleq [y_1, y_2, ..., y_m]$, then the pdf of y is,

$$f(y) = \prod_{m=1}^{M} f(y_m) \tag{2.49}$$

Assume there are a total of N categories the ML-ATR algorithm to decide a target category C can be expressed as,

$$\begin{aligned} C &= arg\max_{n=1}^{N} f(y|\gamma = \gamma_n) \\ &= arg\max_{n=1}^{N} \prod_{m=1}^{M} \frac{y_m}{E^2\gamma^2 + \sigma^2} exp(-\frac{y_m^2}{E^2\gamma^2 + \sigma^2}) \end{aligned} \tag{2.50}$$

2.4.6   simulation

For both fluctuating and non-fluctuating targets, we run 10^5 times Monte-Carlo simulation for each kind of target at different levels of SNRs as well as different deployment of sonars. We set 4 kind of targets with different SCS value, as shown in table 2.1 respectively fish 0.02, marine mammals 0.5, Fishing boat 5, Passenger liner and warships 20. Figure 2.6 (a)(b)(c) show the ATR error rate at different SNR of fish, marine mammal and the average error probability of 4 targets for non-fluctuating case while figure 2.7(a)(b)(c) show the ATR error rate at different SNR of fish, marine mammal and the average error probability of 4 targets for non-fluctuating case. From the figure we can find that when there is only one sonar deployed, the error rate is always greater than 10the uniform 16-sonar SSN and 16-nested SSN the ATR error rate is always lower than 10to Skolnik, the radar performance with a probability of

recognition error less than 10with waveform-diversity can achieve a probability of ATR error much less than 10average ATR for all targets. For our nested deployment case, the ATR rate remains at a relative low level even experiencing a low SNR.

Index n	Target	SCS
1	fish	0.02
2	Marine mammal	0.5
3	Fishing Boat	5
4	Passenger liner and warships	20

Table 2.1. SCS Value at Sonar Frequency for 4 Targets

2.4.7 conculsion

In this section, we proposed a ML-CATR estimation algorithm for the underwater nested array senor network, with M+N physical sensors we can achieve the performance of M N virtual sensors. From the simulation result, we found that the nested array sensors performs much better than the muliple and single deployed senors, which means we can use less senors to achieve a better performance.
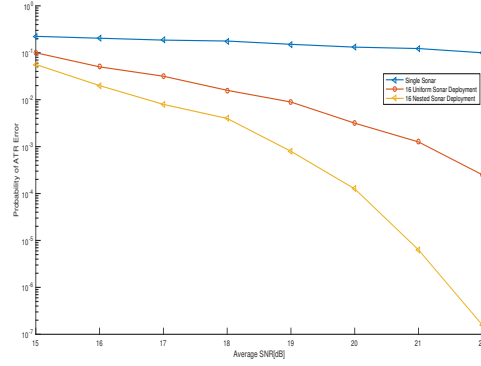
(a)
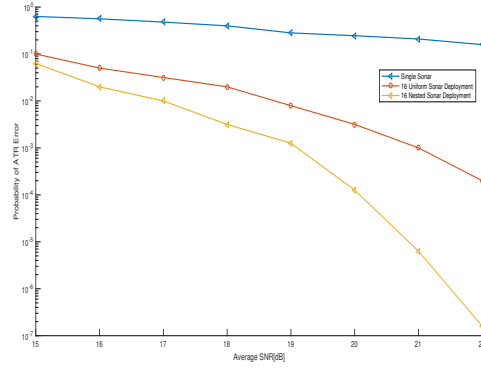
(b)
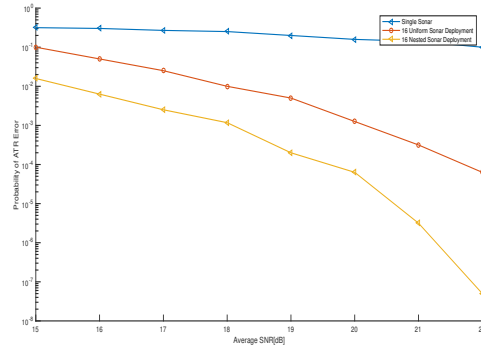
(c)

Figure 2.6. Probability of ATR for non-fluctuating target at different SNR(dB) values.
(a) fish. (b) marine mammals (c) Average probability of ATR for 4 targets.

19
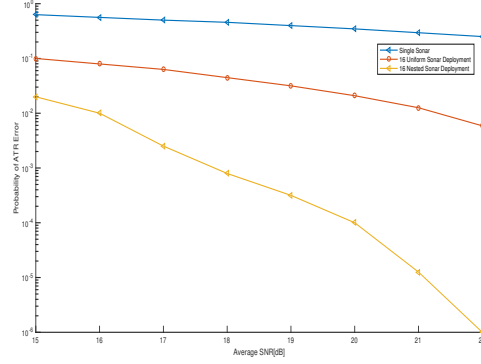
(a)
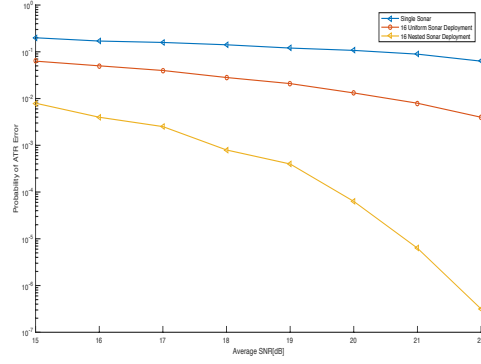
(b)
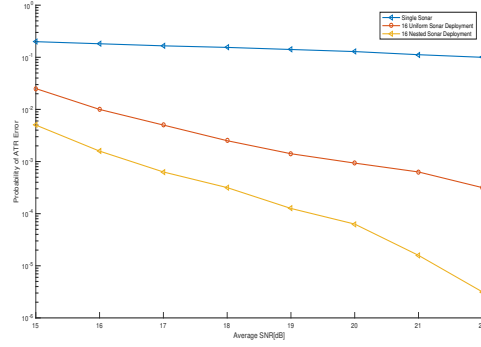
(c)

Figure 2.7. Probability of ATR for fluctuating target at different SNR(dB) values.
(a) fish. (b) marine mammals (c) Average probability of ATR for 4 targets.

CHAPTER 3

Increasing Capacity of Multi-Cell Cooperative Cellular Networks with Coprime

Deployment

3.1   Introduction

With the forthcoming 500 million connections and explosion of mobile broad-band data, heterogeneous networks with a combined approach including improving, densifying and finding better deployment of the cells are becoming the future way to enhance network capacity and performance [42].

Several studies have addressed the cell planning and interference issues in the past. In [43], different symmetric cell deployment strategies have been studied based on inter-site distance and it is concluded that the network capacity can be enhanced through denser deployment of cells. In [44] the authors propose to deploy a massive amount of small cells in order to increase the total capacity and reduce the energy consumption.

However, when the cells are deployed in a super dense way, the inter-cell interference problem would become dominant. In a high interference scenario with many line-of-sight (LOS) interferers around, keep adding cells regardless of the surrounding environment will not always help to improve the network performance.[45]

Hence, finding better deployment of BSs and increasing the level of collaboration would be a better way to achieve higher capacity. In this paper, a novel coprime distributed network is proposed which can increasing the degree of freedom of the co-arrays to reduce the number of physical sensor while maintaining the same performance. The work [47] introduced this theorem into multi-dimensions. In [46], another

sparse deployment method named nested-array was introduced.

The rest of the paper is organized as follows. In Section 2, we give a brief intro-
duction of coprime arrays system and the system model. In Section 3, we study the
sum-rate capacity of the designed system. In Section 4, Monte Carlo simulation result
is provided. The conclusion is drawn in Section 5.

3.2 Preliminary and Model Description

1. *2D Coprime Co-Array* We will firstly introduce several concepts about multidi-
   mensional lattice, which is the basic knowledge to coprime co-array mentioned
   in [47].

   Given a D × D singular matrix V, consider the set of all D × 1vectors of the
   form

   $$t = Vn \tag{3.1}$$

   where n are integer vectors (vectors with integer entries n_i). This set of all is
   called the lattice generated by V and is denoted as LAT(V). The set of all D ×
   1 vectors of the form Vx, where x $\in [0, 1)^D$ (i.e., where the elements of x satisfy
   $0 \le x_i \le 1$), is said to be the fundamental parallelepiped of V, and is denoted
   as FPD(V). Similarly the symmetric parallelepiped SPD(V) is the set of vectors
   Vx with $x \in (-1, 1)^D$. To visualize these definitions, consider the 2-D example
   where V is 2 × 2 and can be written as

   $$V = [v_1 \quad v_2]. \tag{3.2}$$

   Some important points to recall are as follows:

22

1) the volume of FPD(V) (area in 2-D) is equal to $\mid detV \mid$;

2) thus, the number of lattice points generated by V per unit volume (lattice density) is equal to $1/\mid detV \mid$; larger the determnant, smaller is the density of lattice points;

3) LAT(V) is the same as LAT(VE) for any integer matrix E with det E $=\pm1$

Theorem 1. Coprime Co-arrays in 2D: Assume the $2 \times$ nonsigular integer matrixes M and N are commuting and coprime. Then:

1) given any integer vector k, there exist integer vectors $n_1 and n_2$ such that $k = Mn_1 - Nn_2$ holds; the co-array contains all integer vectors, if $n_1 and n_2$ are allowed to vary over all integer vectors;

2) let the integer vectors $n_1 \quad and \quad n_1'$ be restricted to FPD(N) and $n_2 \quad and \quad n_2'$ restricted to FPD(M); then

$$Mn_1 - Nn_2 \neq Mn_1' - N'n_2 \tag{3.3}$$

as long as $(n_1, n_2) \neq (n_1' - Nn_2')$;

3) the integer vector Mn_1 and Nn_2 are distinct when the integers n_1 and n_2 are such that $n_1 \in FPD(N)$ and $n_2 \in FPD(M)$, unless $n_1 = n_2 = 0$.

Theorem 2. Generating All Integer Vectors in FPD(MN): Assume M and N are commuting, coprime, and nonsigular D$\times$ D integer matrixes, and consider the difference $k = Mn_1 - Nn_2$. With $n_1 \in FPD(2N) and n_2 \in$ FPD(M), all integers $k \in$ FPD(MN) can be generated. Similarly, with $n_1 \in$ FPD(N) and $n_2 \in$ SPD(M), all integers $k \in$ FPD(MN) can be generated.

2. *Sum-rate Capacity for Multi-Cell Processing*

The ergodic per-cell sum-rate capacity is given by [48]

$$C(P) = \frac{1}{L}E[log_2(I_L + PH_LH_L^*)] \tag{3.4}$$

Where P is the transmit power of a single user, and the expection is taken with respect to fading coefficients H_L.

The matrix $H_LH_L^*$ is an $L\times$ L matrix given by

$$[H_LH_L^*]_{m,n} = \begin{cases} a_ma_m^* + b_mb_m^* & m = n \\ b_ma_n^* & n = (m-1) \quad modL \\ a_mb_n^* & n = (m+1) \quad modL \\ 0 & otherwise \end{cases} \tag{3.5}$$

3. *System Model*

Figure 1 and Figure 2 demonstrate the distribution of BSs in a 2D coprime array method described in Section 2.1. Where:

$$M = \begin{bmatrix} 1 & 1 \\ -1 & 4 \end{bmatrix} \quad and \quad N = \begin{bmatrix} 2 & 1 \\ -1 & 5 \end{bmatrix} \tag{3.6}$$

As, **M - N = I**, M and N are coprime.

Every dot in Figure 1 stands for a physically deployed macrocell and Figure 2 is the virtual BSs generated by the physical BSs. Every cell has K users. The vector baseband representation of signals received at the BSs is given as

$$y = Hx + n, \tag{3.7}$$

24
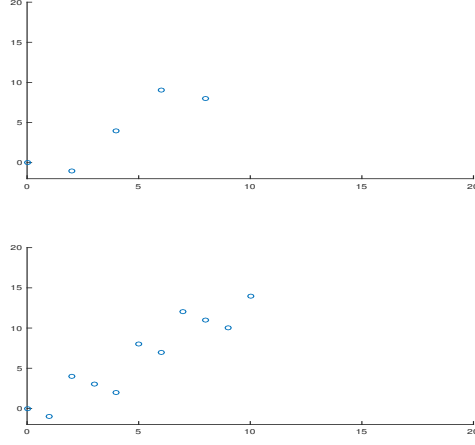
Figure 3.1. The array generated by $Mn_1, n_1 \in FPD(N)$, and $Nn_2, n_2 \in FPD(M)$.

where H is the channel transfer matrix

$$
H = \begin{bmatrix}
a_0 & 0 & 0 & \cdots & 0 & b_0 \\
b_1 & a_1 & 0 & \cdots & 0 & 0 \\
0 & b_2 & a_2 & \cdots & 0 & 0 \\
\vdots & \vdots & \vdots & \ddots & \vdots & \vdots \\
0 & 0 & 0 & \cdots & a_{L-2} & 0 \\
0 & 0 & 0 & \cdots & b_{L-1} & a_{L-1}
\end{bmatrix}
\tag{3.8}
$$

where a_m, b_m are channel coefficients experienced by the K users from the corresponding M and N BSs.

3.3   Sum-rate Capacity of Coprime Distributed Cooperative Networks

4. *Invariance of the Difference Co-array* The difference coarray generated from the coprime array can be expressed as:

$$
k = Mn_1 - Nn_2
\tag{3.9}
$$

25
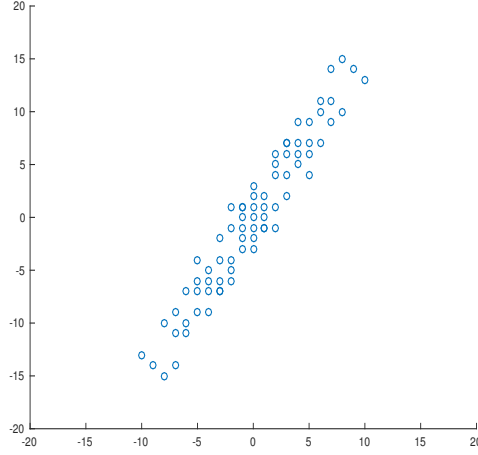
Figure 3.2. $The union of elements in Mn_1 - Nn_2 and Nn_2 - Mn_1.$

The correlation between the any two array elements is

$$R(k) = E[x(Mn_1)x^*(Nn_2)] = E[x(n)x^*(n-k)] \tag{3.10}$$

The received signal vector

$$y_{m,n} = \sum_{k=1}^{k} a(\theta_k)s_k + n_k \tag{3.11}$$

where s_k denotes the signal waveform vector, n_k denoted a i.i.d. Gaussian noise. $a(\theta_k) = [1, e^{-j\frac{2\pi}{\lambda}u_2 sin(\theta_k)}, \cdots, e^{-j\frac{2\pi}{\lambda}u_{2M+N-1} sin(\theta_k)}]^T$, The covariance matrix of received signal vector can be expressed as

$$R = Ey(l)y^*(l) = \sum_{k=1}^{k} \sigma_k^2 a(\theta_k)a^H(\theta_k) + \sigma_n^2 \mathbf{I} \tag{3.12}$$

The covariance matrix will be

$$\hat{R} = \frac{1}{L}\sum_{l=1}^{L} y(l)y^*(l) \tag{3.13}$$

Taking the average of R,

$$\hat{R}^2 = \frac{1}{MN}\sum_{m=0}^{M}\sum_{n=0}^{n} R \tag{3.14}$$

26
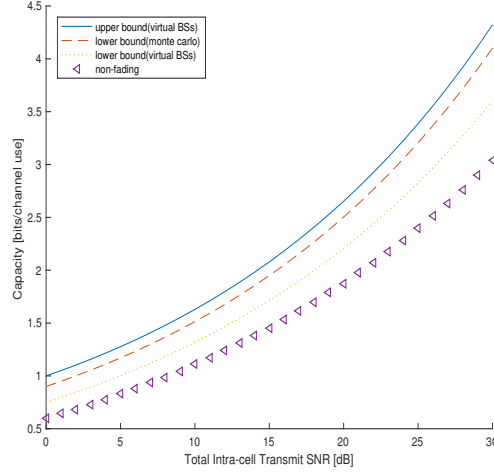
Figure 3.3. Per-cell Sum Rate Capacity for K $= 100$, $\varepsilon = 0.1$.

The covariance matrix of signal has the same form as $\hat{R}^2$ Therefore, the coprime distributed BSs have a degree of freedom of O(MN), with O(M+N) physical BSs.

5. AWGN Channel Assume all fading coefficients in non-fading channels to be 1, all transmission schemes with equal intra-cell power achieve the same throughput. From (5) we can derive that the uplink average per-cell sum rate without fading is

$$C(P) = \frac{1}{L} \sum_{l=0}^{L} log_{10}(1 + 2KP(1 + cos(2\pi\frac{l}{L})))$$
(3.15)

The average per-cell sum-rate capacity with Rayleigh fading is

$$C(P) = \frac{1}{L} \sum_{l=0}^{L-1} long_{10}(1 + 2KP(m_2 + |m_1|^2 cos(2\pi\frac{l}{L})))$$
(3.16)

3.4 Simulation Result

Figure 3.3 and Figure 3.4 show the channel capacity under the different intra-cell transmission power. Lower bounds and upper bounds are also analyzed

27
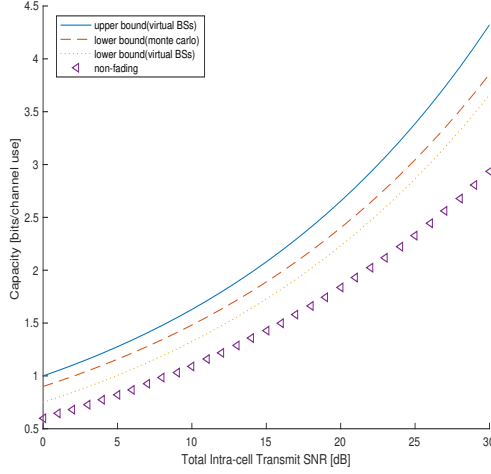
Figure 3.4. Per-cell Sum Rate Capacity for K = 100, $\varepsilon = 0.5$.

with K=100 per cell. Figure 8 shows lower bound for ε=0.1 and figure 9 shows it for ε=0.5.

In fig. 10, we compared the sum-rate capacity between coprime deployment and uniform deployment under Rayleigh fading and non-fading cases with the same number of physical BSs. We observe that the coprime deployment has a 7 times performance improvement comparing to the uniform deployment for both the Rayleigh fading and non-fading cases.

3.5 Conclusion and Future Works

In this paper, we apply the coprime-array algorithm into BSs depolyment case which is a combination of O(M+N) BSs distributed over nonseparable lattices, whose difference co-array can give rise to a much larger 2D array with O(MN) BSs on the dense lattice. Which means that with M+N physical BSs we can achieve the performance of MN BSs. From the simulation result, we find that the coprime array deployed BSs performs much better than the uniform de-
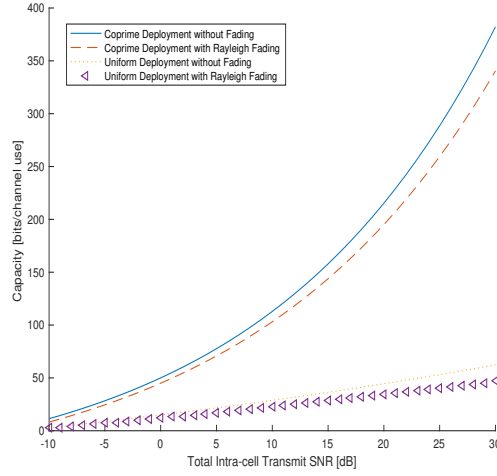
Figure 3.5. Sum-Rate Capacity Comparison between Coprime and Uniform Deployment.

ployed BSs. Which means we can use less number of BSs to achieve a better performance. Meanwhile, there are still some open question beyond this work, including resource allocation, beamforming, interference, the optimal choice of the generate matrix.

CHAPTER 4

Sense-through-Foliage Target Detection Using DCT and UWB Radar Sensor
Networks

4.1   Introduction

UWB radars are used nowadays for different applications such as subsurface
sensing, classification of aircrafts, collision avoidance, etc. In all of these applica-
tions the ultra-high resolution of UWB radars is essentially used [62]. UWB radar
emissions are at a relatively low frequency-typically between 100 MHz and 3 GHz.
Additionally, the fractional bandwidth of the signal is very large (greater than 0.25).
In this definition, bandwidth means the difference between the highest and lowest
frequencies of interest and contains about 95% of the signal power [39][40]. Such
radar sensor has exceptional range resolution that also has an ability to penetrate
many common materials (e.g., walls). Law enforcement personnel have used UWB
ground penetrating radars (GPRs) for at least a decade. In this chapter, we will
study sense-through-foliage target detection using UWB radars.

Like the GPR, sense-through-foliage radar takes advantage of UWB's very fine
resolution (time gating) and low frequency of operation. In [21], Kapoor et al stud-
ied the detection of targets obscured by a forest canopy using a UWB radar. They
observed that the forest clutter observed in the radar imagery is a highly impulsive
random process that is more accurately modeled with the alpha-stable processes as
compared with Gaussian, Weibull, and K-distribution models. With this more accu-
rate model, segmentation was performed on the imagery into forest and clear regions.
Further, a region-adaptive symmetric alpha stable (SαS) constant false-alarm rate

(CFAR) detector was introduced and its performance is compared with the Weibull and Gaussian CFAR detectors. The approach in [21] is a statistical model based approach. In this chapter, we are interested in a non-statistical model-based approach for UWB sense-through-foliage target detection, and we will apply our expertise in signal processing, data fusion, sensor networks, etc to achieve effective sense-through-foliage technology. In [25], sense-through-wall human detection was studied based on UWB radar sensors using standard deviation approach. In [27], multi-step information fusion was applied to sense-through foliage target detection, and information theoretical approach [24] was applied to opportunistic sensing in sense-through foliage target detection. In [23], some preliminary work on sense-through-foliage based on discrete cosine transform was proposed. In this chapter, we are interested in investigating more features from sense through foliage signals and extracting as much information as possible for data fusion in radar sensor networks.

The data fusion in radar sensor networks needs waveform diversity combining. Most existing works on waveform design and selection are focused on single radar or sonar system. In 1974, Fitzgerald [6] demonstrated the inappropriateness of selection of waveforms based on measurement quality alone: the interaction between the measurement and the track can be indirect, but must be accounted for. Since then, extensive works on waveform design have been reported. Bell [4] used information theory to design radar waveforms for the measurement of extended radar targets exhibiting resonance phenomena. In [3], the singularity expansion method was used to design discriminant waveforms such as K-pulse, E-pulse, and S-pulse. Sowelam and Tewfik [36] developed a signal selection strategy for radar target classification, and a sequential classification procedure was proposed to minimize the average number of necessary signal transmissions. Intelligent waveform selection was studied in [2][8], but the effect of Doppler shift was not considered. In [12], time-frequency-

based generalized chirps were used as waveform for detection and estimation. In [11], the performance of constant frequency (CF) and linear frequency modulated (LFM) waveform fusion from the standpoint of the whole system was studied, but the effect of clutter was not considered. In [37], a new time-frequency signal decomposition algorithm based on the S-method was proposed and evaluated on the high-frequency surface-wave radar (HFSWR) data, and demonstrated that it provided an effective way for analyzing and detecting maneuvering air targets with significant velocity changes, including target signal separation from the heavy clutter. In [38], CF and LFM waveforms were studied for a sonar system, but it was assumed that the sensor is non-intelligent (i.e., waveform can't be selected adaptively). All the above studies and design methods focused on the waveform design or selection for a single active radar or sonar system. In [33], cross-correlation properties of two radars were briefly mentioned and the binary coded pulses using simulated annealing [5] are highlighted. However, the cross-correlation of two binary sequences such as binary coded pulses (e.g. Barker sequence) is much easier to study than that of two analog radar waveforms. In [10], waveform design and diversity was studied with clear performance gain. In this chapter, we focus on the waveform diversity and design for radar sensor networks, as well as information fusion for target detection.

The rest of this chapter is organized as follows. In Section 2, we summarize the measurement and collection of data we used in this chapter. In Section 3, we propose a discrete-cosine-transform (DCT) based approach for sense-through-foliage target detection with good signal quality. In Section 4, we propose the theory on waveform design and diversity for radar sensor networks. In Section 5, we propose a radar sensor network (RSN) and DCT-based approach for sense-through-foliage target detection when the signal quality is poor. We conclude this chapter and discuss some future research topics in Section 6.

4.2 Sense-through-Foliage Data Measurement and Collection

The experiments were performed by Virtual Machines Company supported by Air Force Research Lab via FOPEN Phase 2 Field Test project, and the measurements were taken on the grounds of Virtual Machines Company in Holliston, Massachusetts [15]. The foliage experiment was constructed on a seven-ton man lift, which had a total lifting capacity of 450 kg. The limit of the lifting capacity was reached during the experiment as essentially the entire measuring apparatus was placed on the lift. The principle pieces of equipment secured on the lift are listed below:

- Dual Antenna mounting stand

- Two antennas

- Rack system (2)

- Barth pulser

- Tektronix model 7704 B oscilloscope

- IBM laptop

- HP signal Generator

- Custom RF switch and power supply

- Weather shield (small hut)

Figure 4.1 shows the experiment under a weather shield that was constructed on the lift. The weather shield was needed to protect the equipment hoisted up with the lift. A negative side effect of this weather shield was to provide a significant sail area at the maximum lever arm relative to the lift stabilizing jacks on the ground. Lift stabilization was achieved using cables and anchor points. A system of 4 tethers was used under gusty conditions. The transmit and receive rotating platform systems were built using heavy gauge Unistruts, thrust bearings, and roller bearings for the multiple axes of freedom. The importance of the rigidity of the antenna mounts

Figure 4.1. This figure shows the lift with the experiment. The antennas are at the far end of the lift from the viewer under the roof that was built to shield the equipment from the elements. This picture was taken in September with the foliage largely still present. The cables coming from the lift are a ground cable to an earth ground and one of 4 tethers used in windy conditions. .

the and axis of rotation was in the establishment and maintenance of the antenna alignment during the measurement.

The experimental target was a trihedral reflector with a slant length of 1.5 meters (as shown in Fig. 4.2). Throughout this work, a Barth pulse source (Barth Electronics, Inc. model 732 GL) was used. The pulse generator uses a coaxial reed switch to discharge a charge line for a very fast rise time pulse outputs. The model 732 pulse generator provides pulses of less than 50 picoseconds (ps) rise time, with amplitude from 150 V to greater than 2 KV into any load impedance through a 50 ohm coaxial line. The generator is capable of producing pulses with a minimum width of 750 ps and a maximum of 1 microsecond. This output pulse width is determined by charge line length for rectangular pulses, or by capacitors for 1/e decay pulses. The data collections were extensive. 20 different positions were used, and 35 independent collections were performed at each position.

Figure 4.2. The target (a trihedral reflector) is shown on the stand at 300 feet from the lift..

For the data we used in this chapter, each sample is spaced at 50 picosecond interval, and 16,000 samples were collected for each collection for a total time duration of 0.8 microseconds at a rate of approximately 20 Hz. We considered two sets of data from this experiment. Initially, the Barth pulse source was operated at only 1 KW peak power and the system was not sufficiently loaded for repeatable charge control pulse-to-pulse. Significant pulse-to-pulse variability was noted for these collections. In this set of experiments, 35 pulses reflected signal were averaged for each collection. The scheme for the sense-through-foliage target detection with "poor" signal quality will be presented in Section 3.

This problem was remedied by running the pulser at higher power while protecting the radiating antenna using a non-distorting attenuator Barth 3dB attenuator model number 142-NMFP-3. Pulse production stability was very important to this measurement effort. Pulse-to-pulse differences, if any were observed, should be due to changes in the foliage or changes in the transmitter-receiver positions relative to the foliage and target. When operated at the higher amplitudes it was noted that the

35

pulse source was very stable. In this set of experiments, 100 pulses reflected signals were averaged for each collection to average the variation because of the movement of foliage. The scheme for target detection with "good" signal quality will be presented in Section 4.

4.3 Sense-through-Foliage Target Detection with Good Signal Quality: A DCT-based Approach

In Fig. 4.3, we plot two collections with good signal quality, one without target on range (Fig. 4.3a) and the other one with target on range (Fig. 4.3b and target appears at around sample 13,900). To make it more clear to the readers, we provide expanded views of traces (with target) from sample 13,001 to 15,000 for the above two collections in Figs. 4.4a and 4.4b. Since there is no target in Fig. 4.4a, it can be treated as the response of foliage clutter. It's quite straightfoward that the target response will be the echo difference between Fig. 4.4b and Fig. 4.4a, which is plotted in Fig. 4.4c. However, it's impossible to obtain Fig. 4.4a (clutter echo) in practical situation if there is target on range. The challenge is how to make target detection based on Fig. 4.4b (with target) or Fig. 4.4a (no target) only?

Observe Fig. 4.4b, for samples where target appears (around sample 13,900), the sample strength changes much abruptly than that in Fig. 4.4a, which means echo from target contains more AC values than that without target. Motivated by this, we applied Discrete Cosine Transform (DCT) to the echos $x(iM + n)$ ($n = 0, 1, 2, \cdots, N-1$) where N is the DCT window length, M is the step size of each DCT window, and i is the window index. Let $x(n, i) \leq x(iM + n)$

$$X(K, i) = \sum_{n=0}^{N-1} x(n, i) \cos(\frac{2\pi}{N} nK) \qquad (4.1)$$

36

then we cumulate the power of AC values (for $K > 2$)

$$P(i) = \sum_{K=3}^{N-1} X(K,i)^2 \qquad (4.2)$$

For $N = 100$ and $M = 10$, we plot the power of AC values $P(i)$ versus iM (time domain sample index) in Figs. 4.5a and 4.5b for the above data sets in Figs. 4.4a and 4.4b respectively. Observe that in Fig. 4.5b, the power of AC values (around sample 13,900) where the target is located is non-fluctuating (monotonically increase then decrease). Although some other samples also have very high AC power values, it is very clear that they are quite fluctuating and the power of AC values behave like random noise because generally the clutter has Gaussian distribution in the frequency domain [63]. Based on our simulations, the window length N in DCT affects the performance of the target detection. The appropriate N should be the length of target impulse response with strong signal strength (see Fig. 4.4c). This depends on target size, UWB signal resolution, and propagation environment.

We compared our DCT-based approach to the scheme proposed in [97]. In [97], 2-D image was created via adding voltages with the appropriate time offset. In Figs. 4.6a and 4.6b, we plot the 2-D image created based on the above two data sets (from samples 13,800 to 14,200). However, it's not clear which image shows there is target on range.

We also compared our approach to the matched filter approach. The matched filter is by definition a filter in the radar receiver designed to maximize the SNR at its output. The impulse response of the filter having this property turns out to be a replica of the transmitted waveform's modulation function that has been reversed in time and conjugated [30]. Assume the transmitted waveform is $s(t)$, then the matched filter impulse response $h(t) = s^*(T_M - t)$ The time T_M at which the SNR is maximized is arbitrary, however, $T_M \geq t$ is required for $h(t)$ to be causal. Given

37

the received echo $x(t)$ consisting of clutter, target, and noise components, the output $y(t)$ of the matched filter is given by the convolution between $x(t)$ and $h(t)$

$$y(t) \quad = \quad \int_{-\infty}^{\infty} x(\tau)h(t-\tau)d\tau \qquad (4.3)$$

$$= \quad \int_{-\infty}^{\infty} x(\tau)s^*(\tau + T_M - t)d\tau \qquad (4.4)$$

In this chapter, we choose $T_M = 16001$, and the matched filter outputs for received signal in Fig. 4.3a (without target) and signal in Fig. 4.3b (with target) are plotted in Figs. 4.7a and 4.7b respectively. Since the received echoes plotted in Fig. 4.3a and b are averaged over 100 pulses, the transmitted pulse $s(t)$ in (4.4) is obtained via averaging corresponding 100 transmission pulses and is plotted in Fig. 4.8. Observe Figs. 4.7ab, it's impossible to perform target detection based on the matched filter output.

Why the matched filter approach doesn't work for UWB radar-based target detection? We further studied the UWB channel using CLEAN algorithm [17][14][34]. Based on the transmit pulse in Fig. 4.8 and received echo in Fig. 4.4a, we applied CLEAN algorithm and obtained the UWB channel (plotted in Fig. 4.9). Observe Fig. 4.9, the UWB channel has memory because it's a linear filter. However, the matched filter is derived based on the assumption that the radar channel has no memory. The memory in UWB radar channel causes intersymbol interference of transmit pulse and makes the matched filter approach perform poor.

4.4   Waveform Design and Diversity in Radar Sensor Networks

   1. Co-existence of Radar Waveforms

      In radar sensor networks (RSN), radar sensors interfere with each other and the signal-to-interference-ratio may be very low if the waveforms are not properly designed. In this chapter, we introduce orthogonality as one criterion for wave-

form design in RSN to make radars coexistence. In addition, since the radar channel is narrow-band, we will also consider the bandwidth constraint.

In our radar sensor networks, we choose the CF pulse waveform, which can be defined as

$$x(t) = \sqrt{\frac{E}{T}} \exp(j2\pi\beta t) \quad -T/2 \le t \le T/2 \tag{4.5}$$

where β is the RF carrier frequency in radians per second. In radar, ambiguity function (AF) is an analytical tool for waveform design and analysis, which succinctly characterizes the behavior of a waveform paired with its matched filter. The ambiguity function is useful for examining resolution, side lobe behavior, and ambiguities in both range and Doppler for a given waveform [30]. For a single radar, the matched filter for waveform $x(t)$ is $x^*(-t)$, and the ambiguity function of CF pulse waveform is

$$
\begin{aligned}
A(\tau, F_D) &= \left| \int_{-T/2+\tau}^{T/2} x(t) \exp\left(j2\pi F_D s\right) x^*(t-\tau) dt \right| \\
&= \left| \frac{E \sin[\pi F_D(T-|\tau|)]}{T\pi F_D} \right| \quad -T \le \tau \le T
\end{aligned} \tag{4.6}
$$

We can simplify this AF in the following three special cases:

- When $\tau = 0$,

$$A(0, F_D) = \left| \frac{E \sin(\pi F_D T)}{T\pi(F_D)} \right|; \tag{4.7}$$

- when $F_D = 0$,

$$A(\tau, 0) = \left| \frac{E(T-|\tau|)}{T} \right|; \tag{4.8}$$

- and when $\tau = F_D = 0$,

$$A(0, 0) = E \tag{4.9}$$

Note that the above ambiguity is for one radar only (no coexisting radar).

For radar sensor networks, the waveforms from different radars interfere with each other. We choose the waveform for radar i as

$$x_i(t) = \sqrt{\frac{E}{T}} \exp[j2\pi(\beta + \delta_i)t] \quad -T/2 \leq t \leq T/2 \qquad (4.10)$$

which means that there is a frequency shift δ_i for radar i. To minimize the interference from one waveform to another, optimal values for δ_i should be determined to make the waveforms orthogonal to each other, i.e., let the cross-correlation between $x_i(t)$ and $x_n(t)$ be 0,

$$\int_{-T/2}^{T/2} x_i(t)x_n^*(t)dt = \frac{E}{T} \int_{-T/2}^{T/2} \exp[j2\pi(\beta + \delta_i)t] \exp[-j2\pi(\beta + \delta_n)t]dt \qquad (4.11)$$

$$= E\mathrm{sinc}[\pi(\delta_i - \delta_n)T] \qquad (4.12)$$

If we choose

$$\delta_i = \frac{i}{T} \qquad (4.13)$$

where i is a dummy index, (4.12) can be written as

$$\int_{-T/2}^{T/2} x_i(t)x_n^*(t)dt = \begin{cases} E & i = n \\ 0 & i \neq n \end{cases} \qquad (4.14)$$

Therefore choosing $\delta_i = \frac{i}{T}$ in (4.10) yields orthogonal waveforms, i.e., the waveforms can coexist if the carrier spacing is a multiple of $1/T$ between two radar waveforms. In other words, orthogonality amongst carriers can be achieved by separating the carriers by a multiple of the inverse of waveform pulse duration. With this design, all the orthogonal waveforms can work simultaneously. However, there may exist time delay and Doppler shift ambiguity which may interfere with other waveforms in RSN.

2. Interferences of Waveforms In Radar Sensor Networks

(a) RSN with Two Radar Sensors We are interested in analyzing the interference from one radar to another if there exist time delay and Doppler shift. For a simple case where there are two radar sensors (i and n), the ambiguity function of radar i (considering the interference from radar n) is

$$
\begin{aligned}
A_i(t_i, t_n, F_{D_i}, F_{D_n}) &= \left| \int_{-\infty}^{\infty} [x_i(t)\exp(j2\pi F_{D_i}t) + x_n(t - t_n)\exp(j2\pi F_{D_n}t)]x_i^*(t - t_i)dt \right| \quad (4.15) \\
&\leq \left| \int_{-T/2+\max(t_i,t_n)}^{T/2+\min(t_i,t_n)} x_n(t - t_n)\exp(j2\pi F_{D_n}t)x_i^*(t - t_i)dt \right| \\
&\quad + \left| \int_{-T/2+t_i}^{T/2} x_i(t)\exp\left(j2\pi F_{D_i}t\right)x_i^*(t - t_i)dt \right| \quad (4.16) \\
&= \left| \int_{-T/2+\max(t_i,t_n)}^{T/2+\min(t_i,t_n)} x_n(t - t_n)\exp(j2\pi F_{D_n}t)x_i^*(t - t_i)dt \right| \\
&\quad + \left| \frac{E\sin[\pi F_{D_i}(T - |t_i|)]}{T\pi F_{D_i}} \right| \quad (4.17)
\end{aligned}
$$

To make the analysis easier, it is generally assumed that the radar sensor platform has access to the Global Positioning Service (GPS) and the Inertial Navigation Unit (INU) timing and navigation data. In this chapter, we assume that the radar sensors are synchronized and that $t_i = t_n = \tau$. Then (4.17) can be simplified as

$$
A_i(\tau, F_{D_i}, F_{D_n}) \approx |E\text{sinc}[\pi(n - i + F_{D_n}T)]| + \left| \frac{E\sin[\pi F_{D_i}(T - |\tau|)]}{T\pi F_{D_i}} \right| \quad (4.18)
$$

We have the following three special cases:

- If $F_{D_i} = F_{D_n} = 0$, and δ_i and δ_n follow (4.13), (4.18) becomes

$$
A_i(\tau, 0, 0) \approx \left| \frac{E(T - |\tau|)]}{T} \right| \quad (4.19)
$$

- If $\tau = 0$, (4.18) becomes

$$
A_i(0, F_{D_i}, F_{D_n}) \approx |E\text{sinc}[\pi(n - i + F_{D_n}T)]| + \left| \frac{E\sin(\pi F_{D_i}T)}{T\pi F_{D_i}} \right| \quad (4.20)
$$

41

- If $F_{D_i} = F_{D_n} = 0$, $\tau = 0$, and δ_i and δ_n follow (4.13), (4.18) becomes

$$A_i(0,0,0) \approx E \qquad (4.21)$$

(b) RSN with M Radar Sensors

Our analysis on an RSN with two radar sensors can be extended to the case of M radars. Assuming that the time delay τ for each radar is the same, then the ambiguity function of radar 1 (considering interferences from all the other $M - 1$ radars with CF pulse waveforms) can be expressed as

$$A_1(\tau, F_{D_1}, \cdots, F_{D_M}) \approx \sum_{i=2}^{M} |E\mathrm{sinc}[\pi(i - 1 + F_{D_i}T)]| + \left| \frac{E \sin[\pi F_{D_1}(T - |\tau|)]}{T\pi F_{D_1}} \right|$$

$$(4.22)$$

Similarly, we have the following three special cases:

- $F_{D_1} = F_{D_2} = \cdots = F_{D_M} = 0$, and the frequency shift δ_i in (4.10) for each radar follows (4.13), then (4.22) becomes

$$A_1(\tau, 0, 0, \cdots, 0) \approx \left| \frac{E(T - |\tau|)}{T} \right| \qquad (4.23)$$

Comparing it against (4.8), we notice that a radar may exist that can get the same signal strength as that of the single radar in a single radar system (no coexisting radar) when the Doppler shift is 0.

- If $\tau = 0$, then (4.22) becomes

$$A_1(0, F_{D_1}, F_{D_2}, \cdots, F_{D_M}) \approx \sum_{i=2}^{M} |E\mathrm{sinc}[\pi(i - 1 + F_{D_i}T)]| + \left| \frac{E \sin(\pi F_{D_1}T)}{T\pi F_{D_1}} \right|$$

$$(4.24)$$

Comparing to (4.7), a radar in RSN has higher interferences when unknown Doppler shifts exist.

- $F_{D_1} = F_{D_2} = \cdots = F_{D_M} = 0$, $\tau = 0$, and δ_i in (4.10) follows (4.13), then (4.22) becomes

$$A_1(0, 0, 0, \cdots, 0) \approx E \qquad (4.25)$$

42

3. Radar Sensor Network for Collaborative Automatic Target Recognition

In RSN with M radars, the received signal for clusterhead (assume it's radar 1) is

$$r_1(u,t) = \sum_{i=1}^{M} \alpha(u) x_i(t - t_i) \exp(j2\pi F_{D_i}t) + n(u,t) \tag{4.26}$$

where $\alpha(u)$ stands for radar cross section (RCS), which can be modeled using non-zero constants for non-fluctuating targets and four Swerling target models for fluctuating targets [30]; F_{D_i} is the Doppler shift of the target relative to waveform i; t_i is the delay of waveform i, and $n(u,t)$ is the additive white Gaussian noise (AWGN). In this chapter, we propose a RAKE structure for waveform diversity combining, as illustrated by Fig. 4.10. The RAKE structure is so named because it reminds the function of a garden rake, each branch collecting echo energy similarly to how tines on a rake collect leaves. This figure summarizes how the clusterhead works. The received signal $r_1(u,t)$ consists of echoes triggered by the waveforms from each radar sensor, and $x_i^*(t - t_i)$ is used to retrieve the amplified waveform from radar i (amplified by the target RCS) based on the orthogonal property presented in Sections 1 and 2, and then this information is time-averaged for diversity combining.

According to this structure, the received $r_1(u,t)$ is processed by a bank of matched filters, then the output of branch 1 (after integration) is

$$
\begin{aligned}
&Z_1(u; t_1, \cdots, t_M, F_{D_1}, \cdots, F_{D_M}) \\
=\ &\int_{-T/2}^{T/2} r_1(u,t) x_1^*(t - t_1) ds \tag{4.27} \\
=\ &\int_{-T/2}^{T/2} [\sum_{i=1}^{M} \alpha_i(u) x_i(t - t_i) \exp(j2\pi F_{D_i}t) + n(u,t)] x_1^*(t - t_1) dt \tag{4.28}
\end{aligned}
$$

Assuming $t_1 = t_2 = \cdots = t_M = \tau$, then based on (4.22),

$$
\begin{aligned}
Z_1(u; \tau, F_{D_1}, \cdots, F_{D_M}) \approx & \sum_{i=2}^{M} \alpha(u) E \mathrm{sinc}[\pi(i - 1 + F_{D_i}T)] \\
& + \frac{\alpha(u) E \sin[\pi F_{D_1}(T - |\tau|)]}{T \pi F_{D_1}} + n(u, \tau) \quad (4.29)
\end{aligned}
$$

Similarly, we can get the output for any branch m ($m = 1, 2, \cdots, M$),

$$
\begin{aligned}
Z_m(u; \tau, F_{D_1}, \cdots, F_{D_M}) \approx & \sum_{i=1, i \neq m}^{M} \alpha(u) E \mathrm{sinc}[\pi(i - m + F_{D_i}T)] \\
& + \frac{\alpha(u) E \sin[\pi F_{D_m}(T - |\tau|)]}{T \pi F_{D_m}} + n(u, \tau) \quad (4.30)
\end{aligned}
$$

Therefore $Z_m(u; \tau, F_{D_1}, \cdots, F_{D_M})$ consists of three parts, namely signal (reflected signal from radar m waveform): $\frac{\alpha(u) E \sin[\pi F_{D_m}(T - |\tau|)]}{T \pi F_{D_m}}$, interferences from other waveforms: $\sum_{i=1, i \neq m}^{M} \alpha(u) E \mathrm{sinc}[\pi(i - m + F_{D_i}T)]$, and noise: $n(u, \tau)$.
We can also have the following three special cases for $|Z_m(u; \tau, F_{D_1}, \cdots, F_{D_M})|$:

- When $F_{D_1} = \cdots = F_{D_M} = 0$,

$$
Z_m(u; \tau, 0, 0, \cdots, 0) \approx \frac{E \alpha(u)(T - |\tau|)}{T} + n(u, \tau) \quad (4.31)
$$

  which means that if there is no Doppler mismatch, there is no interference from other waveforms.

- If $\tau = 0$, (4.30) becomes

$$
\begin{aligned}
& Z_m(u; 0, F_{D_1}, \cdots, F_{D_M}) \\
& \approx \sum_{i=1, i \neq m}^{M} \alpha(u) E \mathrm{sinc}[\pi(i - m + F_{D_i}T)] + \frac{\alpha(u) E \sin[\pi F_{D_m}T]}{T \pi F_{D_m}} + n(u) \quad (4.32)
\end{aligned}
$$

- If $\tau = 0$, and $F_{D_1} = \cdots = F_{D_M} = 0$, (4.30) becomes

$$
Z_m(u; 0, 0, 0, \cdots, 0) \approx E \alpha(u) + n(u) \quad (4.33)
$$

44

Doppler mismatch happens quite often in target search where target velocity is not yet known. However, in target recognition, generally high-resolution measurements of targets in range ($\tau = 0$) and Doppler are available, therefore (4.33) will be used for CATR.

How to combine all the Z_m's ($m = 1, 2, \cdots, M$) is very similar to the diversity combining in wireless communications to combat channel fading, and the combination schemes may be different for different applications. In this chapter, we are interested in applying the RSN waveform diversity to CATR, e.g., recognition that the echo on a radar display is that of an aircraft, ship, motor vehicle, bird, person, rain, chaff, clear-air turbulence, land clutter, sea clutter, bare mountains, forested areas, meteors, aurora, ionized media, or other natural phenomena via collaborations among different radars. Early radars were "blob" detectors in that they detected the presence of a target and gave its location in range and angle, and radar began to be more than a blob detector and could provide recognition of one type of target from another [33]. It is known that small changes in the aspect angle of complex (multiple scatter) targets can cause major changes in the radar cross section (RCS). This has been considered in the past as a means of target recognition, and is called *fluctuation of radar cross section with aspect angle*, but it has not had much success [33]. In [32], a parametric filtering approach was proposed for target detection using airborne radar. In [9], knowledge-based sensor networks were applied to threat assessment. In this chapter, we propose maximum likelihood collaborative automatic target recognition (ML-CATR) algorithms for non-fluctuating targets as well as fluctuating targets.

4.5 Sense-through-Foliage Target Detection with Poor Signal Quality: A Sensor Network and DCT-based Approach

As mentioned in Section 4.2, when the Barth pulse source was operated at low amplitude and the sample values are not obtained based on sufficient pulse response averaging (averaged over 35 pulses for each collection), significant pulse-to-pulse variability was noted and the return signal quality is poor. In Figs. 4.11a and 4.11b, we plot two collections with poor signal quality. Fig. 4.11a has no target on range, and Fig. 4.11b has target at samples around 13,900. We plot the echo differences between Figs. 4.11a and 4.11b in Fig. 4.11c. However, it is impossible to identify whether there is any target and where there is target based on Fig. 4.11c. We observed the DCT-based approach failed to detect target based on one collection. Since significant pulse-to-pulse variability exists in the echos, this motivate us to explore the spatial and time diversity using Radar Sensor Networks (RSN).

In RSN, the radar sensors are networked together in an ad hoc fashion. They do not rely on a preexisting fixed infrastructure, such as a wireline backbone network or a base station. They are self-organizing entities that are deployed on demand in support of various events surveillance, battlefield, disaster relief, search and rescue, etc. Scalability concern suggests a hierarchical organization of radar sensor networks with the lowest level in the hierarchy being a cluster. As argued in [73] [70] [69] [96], in addition to helping with scalability and robustness, aggregating sensor nodes into clusters has additional benefits:

- conserving radio resources such as bandwidth;
- promoting spatial code reuse and frequency reuse;
- simplifying the topology, e.g., when a mobile radar changes its location, it is sufficient for only the nodes in attended clusters to update their topology information;

- reducing the generation and propagation of routing information; and,

- concealing the details of global network topology from individual nodes.

In RSN, each radar can provide their pulse parameters such as timing to their clusterhead radar, and the clusterhead radar can combine the echos (RF returns) from the target and clutter. In this chapter, we propose a RAKE structure for combining echos, as illustrated by Fig. 4.10. The RAKE structure is so named because it reminds the function of a garden rake, each finger collecting echo signals similarly to how tines on a rake collect leaves. The integration means time-average for a sample duration T and it's for general case when the echos are not in discrete values. It is quite often assumed that the radar sensor platform will have access to Global Positioning Service (GPS) and Inertial Navigation Unit (INU) timing and navigation data. In this chapter, we assume the radar sensors are synchronized in RSN. In Fig. 4.10, the echo, i.e., RF response by the pulse of each cluster-member sensor, will be combined by the clusterhead using a weighted average, and the weight w_i is determined by the power of each echo $x_i(n)$ (n is the sample index),
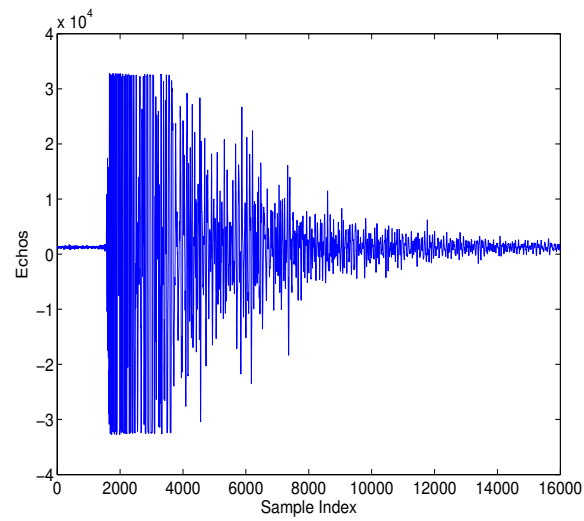
$$w_i = \frac{E_i}{\sum_{i=1}^{M} E_i} \tag{4.34}$$

and

$$E_i = \text{var}(x_i(n)) + [\text{mean}(x_i(n))]^2 \tag{4.35}$$

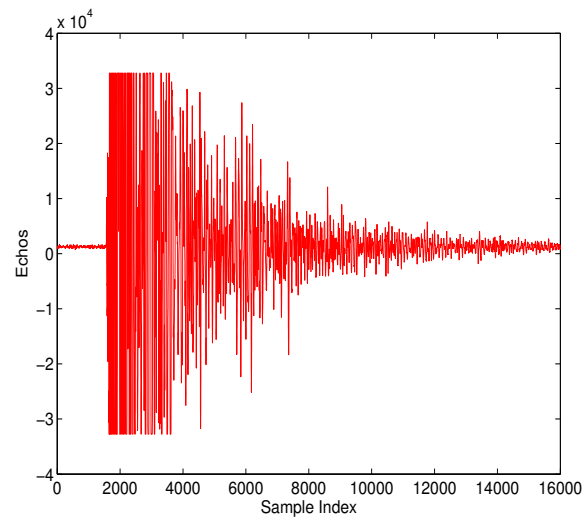We ran simulations for $M = 30$, and plot the power of AC values in Figs. 4.12a and 4.12b for the two cases (with target and without target) respectively. Observe that in Fig. 4.5b, the power of AC values (around sample 13,900) where the target is located is non-fluctuating (monotonically increase then decrease). Although some other samples also have very high AC power values, it is very clear that they are quite fluctuating and the power of AC values behaves like random noise because generally the clutter has Gaussian distribution in the frequency domain.

4.6   Conclusions and Future Works

In this chapter, we proposed a DCT-based approach for sense-through-foliage target detection when the echo signal quality is good, and a sensor network and DCT-based approach when the echo signal quality is poor. A RAKE structure which can combine the echos from different cluster-members is proposed for clusterhead in the RSN. We compared our approach with ideal case when both echos are available, i.e., echos with target and without target. We also compared our approach against the scheme in which 2-D image was created via adding voltages with the appropriate time offset as well as the matched filter-based approach. We observed that the matched filter-based couldn't work well because the UWB channel has memory. Simulation results show that our DCT-based scheme works much better than the existing approach, and our RSN and DCT-based approach can be used for target detection successfully while the ideal case fails to do it. For future works, we will collect more data with different targets and perform automatic target recognition besides target detection.
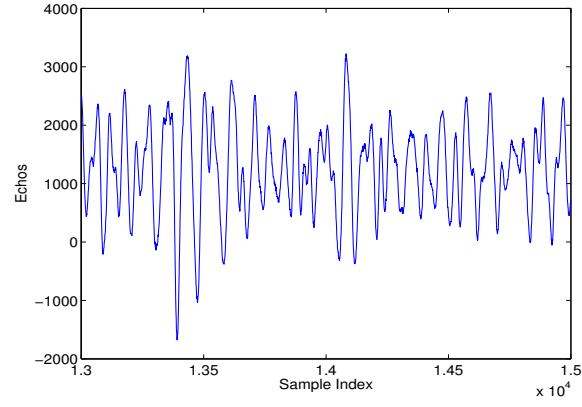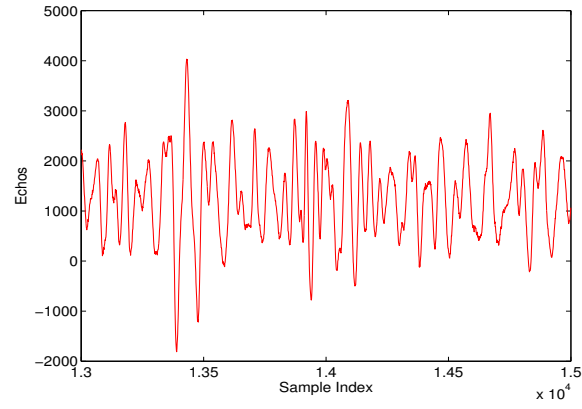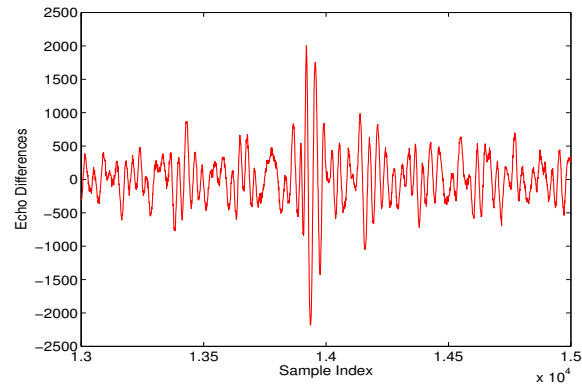
(a)

(b)

Figure 4.3. Measurement with very good signal quality and 100 pulses average. (a) No target on range, (b) with target on range (target appears at around sample 13,900).

Figure 4.4. Measurement with very good signal quality and 100 pulses average. (a) Expanded view of traces (with target) from samples 13,001 to 15,000. (b) Expanded view of traces (without target) from samples 13,001 to 15,000. (c) Echo differences between (a) and (b)..

a

b

Figure 4.5. The power of AC values versus sample index. (a) No target (b) With target in the field..
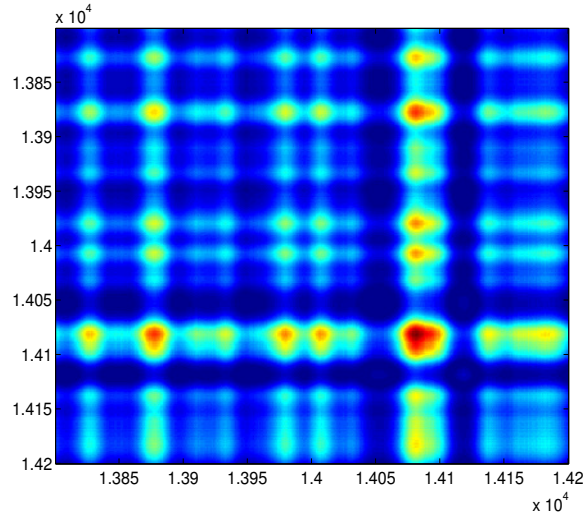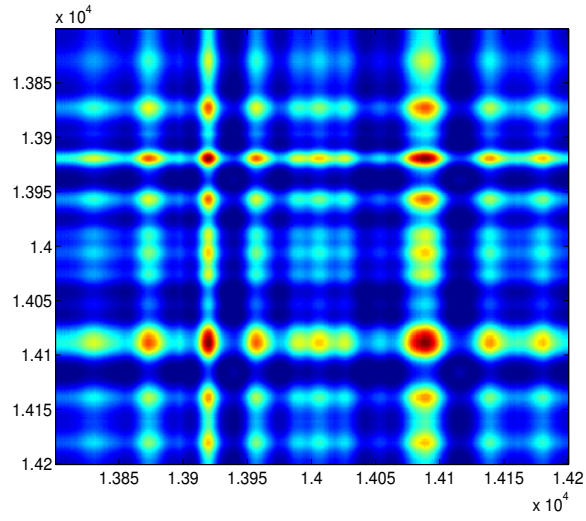
Figure 4.6. 2-D image created via adding voltages with the appropriate time offset. (a) No target (b) With target in the field..
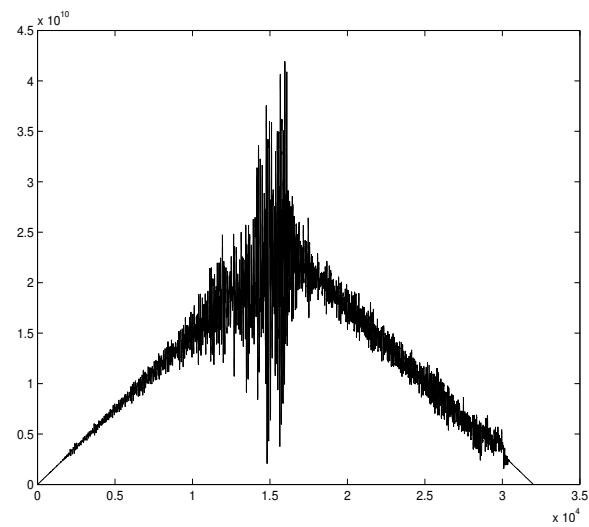
a
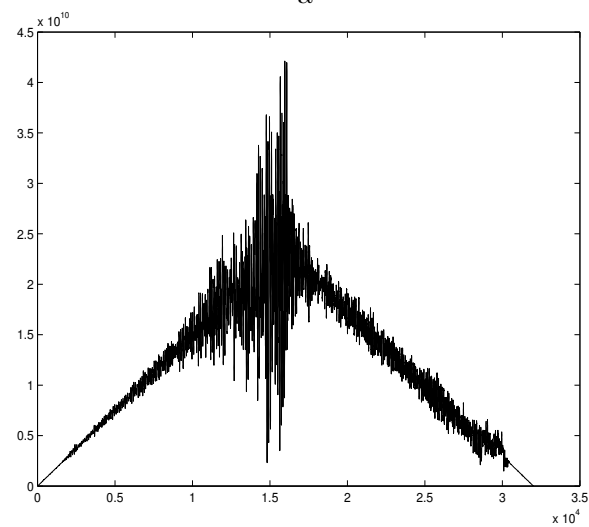
b

Figure 4.7. The matched filter output (a) no target, and (b) with target..
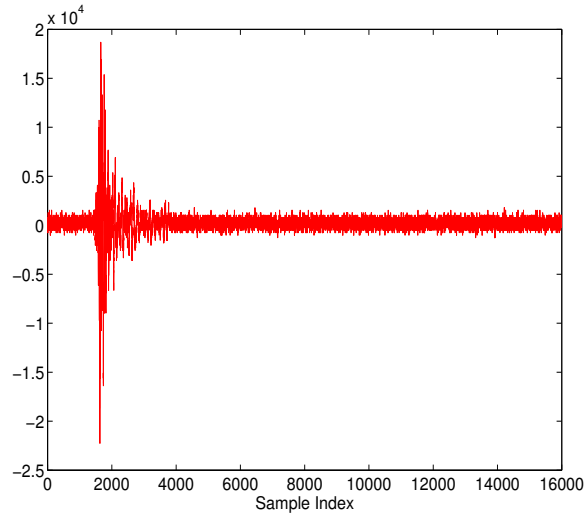
Figure 4.8. UWB radar transmitted pulse (averaged over 100 pulses).
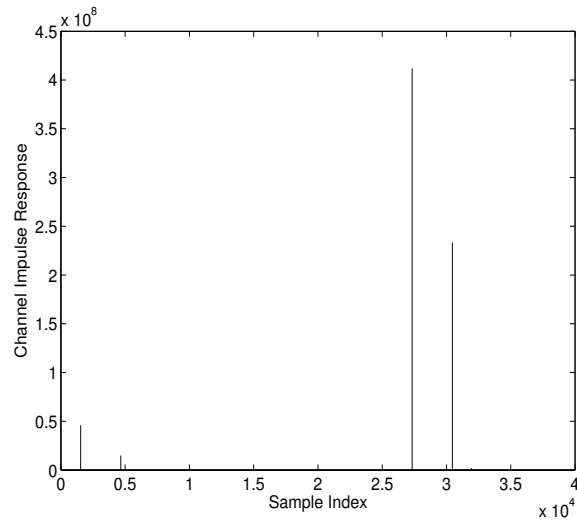
Figure 4.9. The channel impulse responses for UWB channel using CLEAN method.

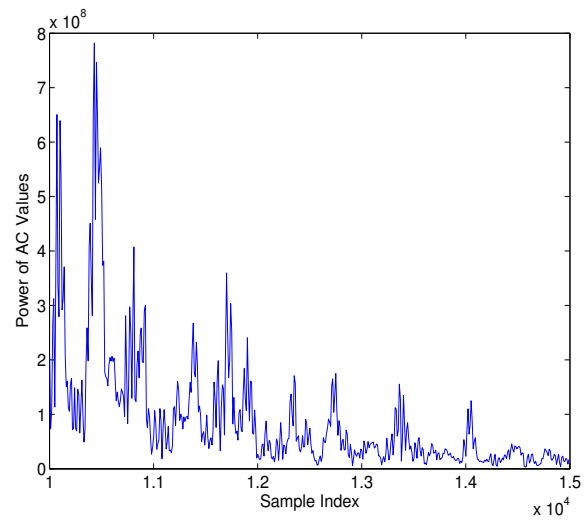54
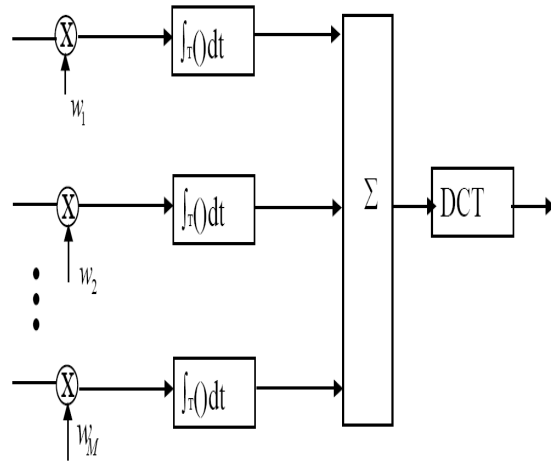
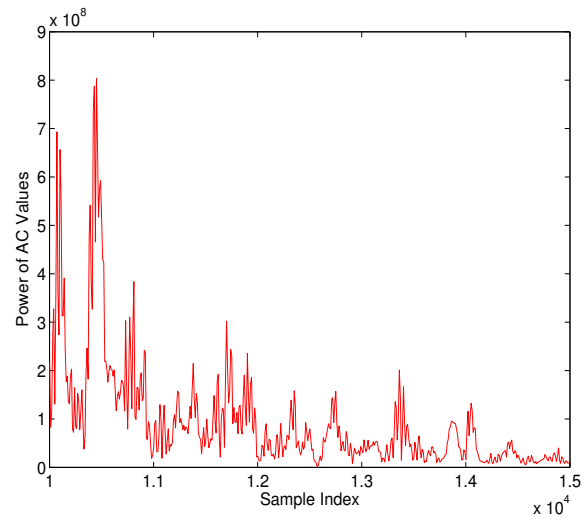Figure 4.10. Echo combining by clusterhead in RSN.
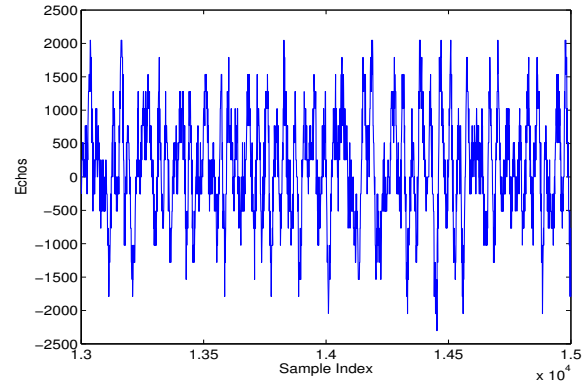
(a)
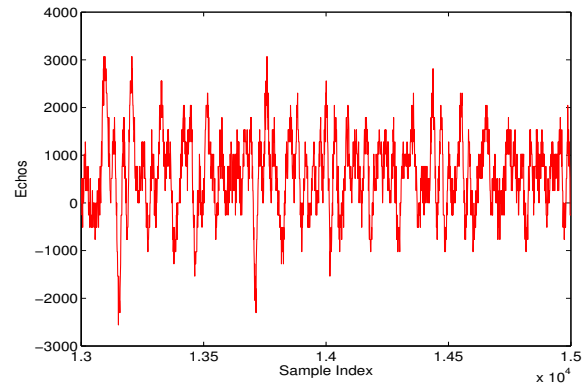
(b)
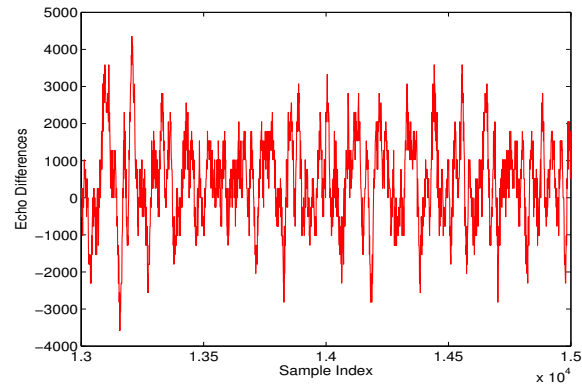
(c)

Figure 4.11. Measurement with poor signal quality and 35 pulses average. (a) Expanded view of traces (no target) from sample 13,001 to 15,000. (b) Expanded view of traces (with target) from sample 13,001 to 15,000. (c) The differences between (a) and (b).
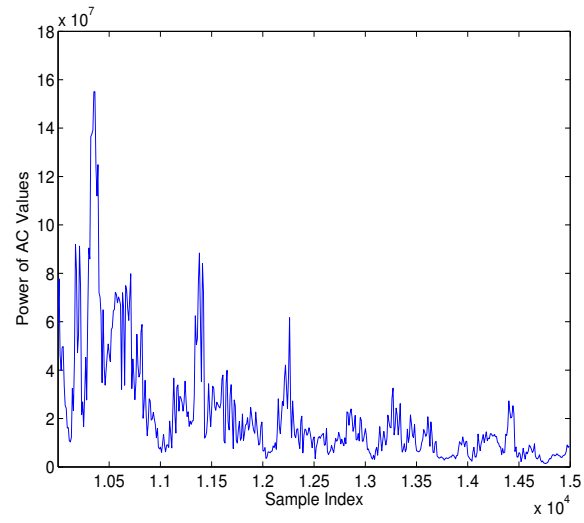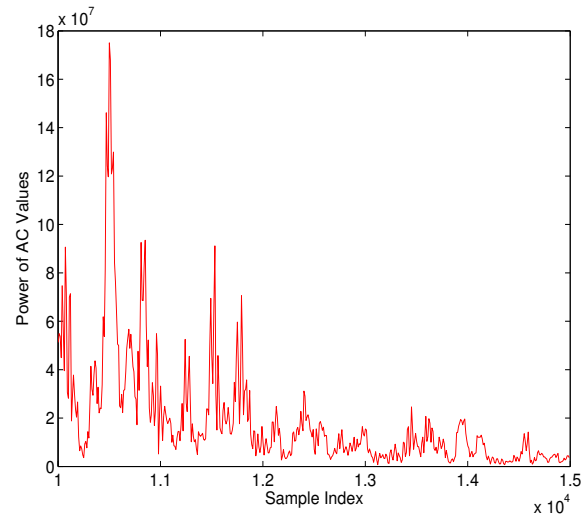
Figure 4.12. Power of AC values based on UWB radar sensor networks and DCT based approach. (a) No target (b) With target in the field.

CHAPTER 5

Sence-through-Foliage Target Detection based on Transfer Entropy Approach using
UWB Radar

5.1   Introduction

Target detection in a strong clutter background is a significant topic of civilian
and military research and applications. The echo of the signal contains information
for the target, the environment as well as the interference and the noise. However,
the non-stationary nature of foliage environment, for instance, doppler shift caused
by leaves and branched makes the target detection more difficult.

In this paper, our goal is to detect the target from the foliage clutter background
based on our knowledge on transfer entropy. The notion of TE is firstly introduced
by T.Schreiber, and then mainly applied into biological system. TE needs relatively
long time series, therefore, it could only applied in systems like neural signal, ECG,
EEG etc[83][82]. Transfer entropy is a method to find the causal relationship of time
series based on probability distribution and Shannon entropy, it is believed that TE
will draw more and more attention along with the era of Big Data arriving.

Comparing to Milimeter-Wave Radar based on the characteristic of foliage tar-
get detection, Ultra-wideband(UWB) radar operate between 300 MHz to 3 GHz with
a large fractional bandwidth greater than 20 percent. UWB is more suitable for this
case. Moreover, the good penetration ability as well as the the high resolution also
give UWB more advantage in term of Sense-through-Foliaged target detection[81].

Some previous works related to target detection or identification based on en-
tropy approach have been conducted. In [84], it introduced and described Shannon

58

entropy and its decomposition from polarimetric SAR datasets, and then gave the procedure of polarimetric SAR data processing. Shannon entropy, other polarization parameters, and polarization decomposition results in the study area were analyzed. [86] proposed an entropy-based H-α decomposition method was applied to analyze fully polarimetric GPR data which were collected from the field. Preliminary analyses showed that this method can be used to classify targets with different polarization scattering properties. It is demonstrated that the application in detecting buried unexploded ordnance which have linear scattering features. Information entropy is also used in range spread target detection in[85]. Entropy is used as a tool for detecting small target in sea clutter.[87]. However none of these studies used target obscured by foliage. In [88] proposed a mutual information based method to detect target in forest. In[93], sense-through-wall human detection was studied based on UWB radar sensors using standard deviation approach. In[92], multi-step information fusion was applied to sense-through foliage target detection, and information theoretical approach[91] was applied to opportunistic sensing in sense-through foliage target detection.

The rest of this chapter is organized as follows. Section II summarizes the measurement of data used in this work. In section III we describe transfer entropy based target detection. Section IV we analyze the simulation result. In section V we conclude our work and discuss future research.

5.2   Sense-through-Foliage Data Measurement and Collection

For this chapter, we use the same Data from last Chapter.

In Fig. 4.3, we plot two collections with good signal quality, one without target on range (Fig. 4.3a) and the other one with target on range (Fig. 4.3b and target appears at around sample 13,900). To make it more clear to the readers, we provide expanded views of traces (with target) from sample 13,001 to 15,000 for the above

two collections in Figs. 4.4a and 4.4b. Since there is no target in Fig. 4.4a, it can be treated as the response of foliage clutter. It's quite straightfoward that the target response will be the echo difference between Fig. 4.4b and Fig. 4.4a, which is plotted in Fig. 4.4c. However, it's impossible to obtain Fig. 4.4a (clutter echo) in practical situation if there is target on range. The challenge is how to make target detection based on Fig. 4.4b (with target) or Fig. 4.4a (no target) only.

5.3 Transfer entropy based Target Detection

Transfer entropy measures how much information the source process provides about state transitions in the target. TE is more adequate (than Mutual Information(MI) or time-delayed MI) for determining the direction of inf. flow between two coupled processes.[89]

Suppose two echoes, X and Y, We define an entropy rate which is the amount of additional information required to represent the value of the next observation of one of the echoes:

$$h_1 = -\sum_{x_{n+1}} p(x_{n+1}, x_n, y_n) log p(x_{n+1}|x_n, y_n) \tag{5.1}$$

Suppose that value of x_{n+1} is not dependent on the current y_n :

$$h_2 = -\sum_{x_{n+1}} p(x_{n+1}, x_n, y_n) lop(x_{n+1}|x_n) \tag{5.2}$$

and,

$$TE_{Y \to X} = h_2 - h_1 \tag{5.3}$$
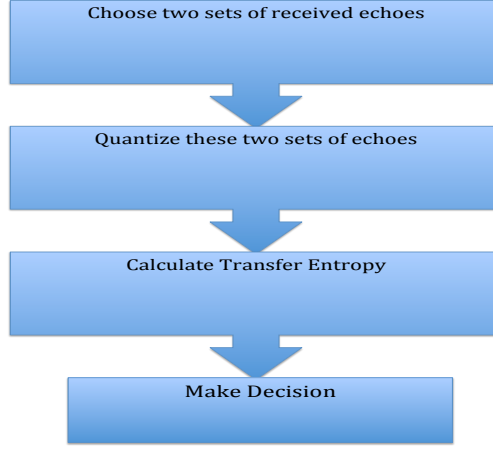
Figure 5.1. The block diagram of target detection process.

$$
\begin{aligned}
TE_{Y \to X} &= \sum p(y_{n+1}, y_n, x_n) log \frac{p(y_{n+1}, y_n, x_n)}{p(y_{n+1}|y_n)p(y_n, x_n)} \\
&= \sum p(y_{n+1}, y_n, x_n) log \frac{p(y_{n+1}, y_n, x_n)}{p(y_{n+1}|y_n)p(y_n, x_n)} \frac{p(y_n)}{p(y_n)} \\
&= \sum p(y_{n+1}, y_n, x_n) log \frac{p(y_{n+1}, x_n, y_n)p(y_n)}{p(y_{n+1}, y_n)p(x_n, y_n)}
\end{aligned}
\tag{5.4}
$$

$$
TE_{X \to Y} = \sum p(x_{n+1}, x_n, y_n) log \frac{p(x_{n+1}, y_n, x_n)p(x_n)}{p(x_{n+1}, x_n)p(y_n, x_n)}
\tag{5.5}
$$

$$
TE_{XY} = TE_{Y \to X} + TE_{X \to Y}
\tag{5.6}
$$

The transfer entropy target detection process is described below:

- Let Q to be the quantized received signal with a particular codebook and partition. Since the calculation of transfer entropy involved the processing in the $O(2^m)$ when 2^m is the quantization level, we try not to quantize too much.

- As we know the target lies at the distance of about 300ft away, therefore, the echoes reflected by the target should be around 13900 sample index. So we choose the sample interval from 12000 to 15000 to make analysis.

61

- Let $N = [N_1, N_2, N_3......N_M]$ set of windows. Where M= length of signal/n and n is the size of the window.

- Transfer Entropy $TE_{Y \to X}$ is calculated for all i=1:M. Here K=1:n, where n is the size of the window.

- Target is detected at the location of $Max(TE_{XY})$

5.4 Simulation

In this paper, we ran 10^3 simulation for each quantization level at a window size of 100 to compare their detection error rate. Fig 6. shows an example of quantized echo with a quantization level of 16. Fig 7. shows the transfer entropy of echoes with target, the target is correctly detected at around 13900. Fig 8. gives the transfer entropy of echoes without target. Finally in Fig 9. we plot the comparison of our proposed algorithm and the existing linear regression approach. We can see from the result our approach is better than the linear regression approach and the performance improves as the quantization level goes up and converge at the quantization level of 64. When the quantization level goes up, more information will be transmitted by the echoes. Transfer entropy reflects the transfer of information, so the accuracy goes up.

5.5 Conclusion and Future Works

In this paper we propose a new algorithm for target detection through foliage based on information theory. Result shows that our approach overperforms some existing approach. In future we can acquire more data and apply transfer entropy based detection into multi target environment or higher dimensional target detection(For example 2D image target detection).
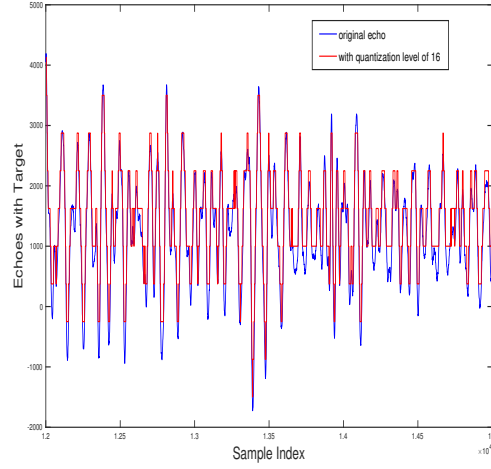
Figure 5.2. Quantized echo and original echo.
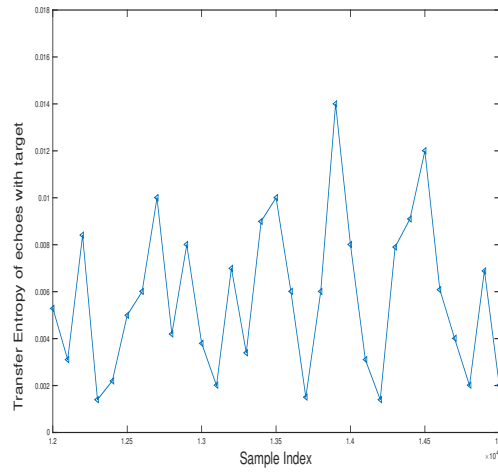
Figure 5.3. Transfer Entropy of Echoes with Target.
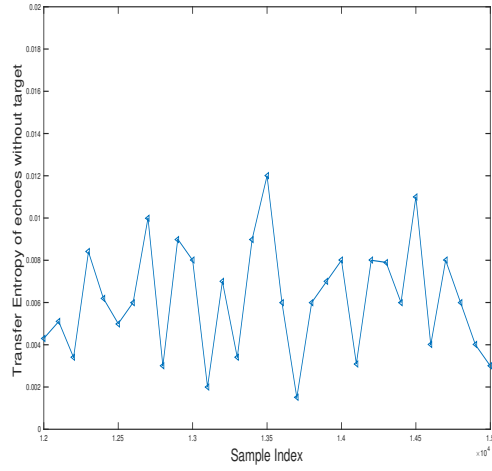
Figure 5.4. Transfer Entropy of Echoes without Target.
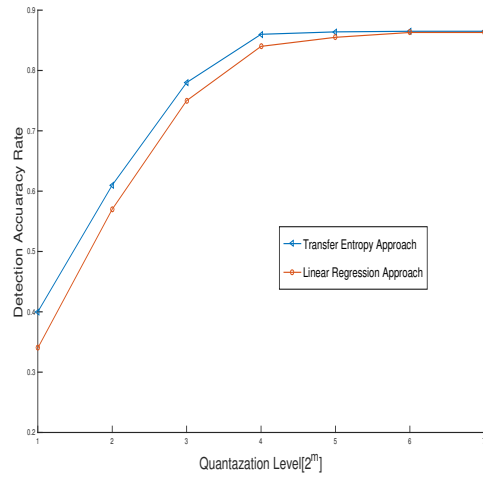
Figure 5.5. Compare with Linear Regression Approach.

CHAPTER 6

Conclusion and Future Work

For Chapter 2, we extend the nested-array algorithm into 3-D underwater case which is a combination of O(M+N) sensors distributed over nonseparable lattices, whose difference co-array can give rise to a much larger 3D array with O(MN) sensors on the dense lattice. Based on the nested-array model, we proposed a ML-CATR estimation algorithm for the underwater nested array senor network. From the simulation result, we find that the nested array sensors performs much better than the multiple and single deployed sensors. Which means we can use less sensors to achieve a better performance.

For the future work which may include but not limited to the optimization deployment of nested-array and also in the case when the numbers of targets is time varying.

For Chapter 3, we apply the coprime-array algorithm into BSs deployment. The feasibility and characteristics for the Co-prime distributed cellular network are discussed in this paper based on a traditional multi-cell model. The model assumes a modified version of soft-handoff scenario, in which each user simultaneously communicates with two BSs. Both the nonfading and Rayleigh fading channels are analyzed in terms of the average per-cell sum-rate capacity and spectrum efficiency. It shows that the invariant of difference co-array is valid to analyze the covariance of channel fading coefficients, which plays an important role to derive the cell capacity. The numeric results also support the correctness of the propositions. We observe that

the co-prime deployment has a 7 times performance improvement comparing to the uniform deployment for both the Rayleigh fading and non-fading cases. A key insight of the present work is that by carefully deploying and scheduling communication between users and different BSs, the cluster of the BSs is able to achieve a much higher capacity compared to the simple collaboration among BSs. On the other hand, there are many open questions in this direction of research, including detailed power allocation and beamforming for the combination of dense array and sparse array, the interference analysis when this Co-prime distributed cellular network is put into a system at large, and the relation between the uplink and downlink channels.

In Chapter 4, we proposed a DCT-based approach for sense-through-foliage target detection. We also applied matched filter approach to sense-through-foliage target detection. We also compared our approach against the scheme in which 2-D image was created via adding voltages with the appropriate time offset. Simulation results show that our DCT-based scheme works much better than the other approaches. We observed that the matched filter-based couldn't work well because the UWB channel has memory. Simulation results show that our DCT-based scheme works much better than the existing approach, and our RSN and DCT-based approach can be used for target detection successfully while the ideal case fails to do it.

For future works, we will collect more data with different targets and perform automatic target recognition besides target detection.

In the last Chapter, we propose a new algorithm for target detection through foliage based on information theory. Result shows that our approach overperforms some existing approach. In future we can acquire more data and apply transfer

entropy based detection into multi target environment or higher dimensional target detection(For example 2D image target detection).

REFERENCES

[1] D. K. Barton, *Radar System Analysis and Modeling*, Artech House, Boston, MA, 2006.

[2] P. Baggenstoss, "Adaptive pulse length correction (APLECORR): a strategy for waveform optimization in ultrawideband active sonar," *IEEE Trans on Oceanic Engineering*, vol. 23, no. 1, pp. 1-11, 1998.

[3] C. E. Baum, et al, "The singularity expansion method and its application to target identification", *Proc. of the IEEE*, vol 79, no. 10, Oct 1991.

[4] M. R. Bell, "Information theory and radar waveform design", *IEEE Trans on Information Theory*, vol. 39, no. 5, pp. 1578-1597, Sept 1993.

[5] H. Deng, "Synthesis of binary sequences with good correlation and cross-correlation properties by simulated annealing," *IEEE Trans on Aerospace and Electronic Systems*, vol. 32, no. 1, Jan 1996.

[6] R. Fitzgerald, "Effects of range-Doppler coupling on chirp radar tracking accuracy," *IEEE Trans on Aerospace and Electronic Systems*, vol. 10, pp. 528-532, July 1974.

[7] R. A. Johnson and E. L. Titlebaum, "Range Doppler Uncoupling in the Doppler Tolerant Bat Signal", *Proc. of IEEE Ultrasonics Symposium*, New York, pp. 64-67, 1972.

[8] D. Kershaw and R. Evans, "Optimal waveform selection for tracking system", *IEEE Trans on Information Theory*, vol. 40, no. 5, pp. 1536-1550, 1994.

[9] Q. Liang, X. Cheng, "KUPS: Knowledge-based Ubiquitous and Persistent Sensor Networks for Threat Assessment", *IEEE Trans on Aerospace and Electronic Systems*, vol. 44, no. 3, July 2008.

[10] Q. Liang, X. Cheng, S. Samn, "NEW: Network-enabled Electronic Warfare for Target Recognition," *IEEE Trans on Aerospace and Electronic Systems*, vol.46, no. 2, pp. 558-568, April 2010.

[11] R. Niu, P. Willett, and Y. Bar-Shalom, "Tracking consideration in selection of radar waveform for range and range-rate measurements", *IEEE Transactions on Aerospace and Electronic Systems*, Vol. 38, No. 2, 2002.

[12] A. Papandreou, G. F. Boudreaux-Bartels, and S. M. Kay, "Detection and estimation of generalized chirps using time-frequency representation", *Twenty-Eighth Asilomar Conference on Signals, Systems and Computers*, vol. 1, pp. 50-54, Oct. 1994.

[13] M. Y. W. Chia, et. al, "Through-wall UWB radar operating within FCC's mask for sensing heart beat and breathing rate," *2005 European Radar Conference*, Oct. 2005, pp. 267 - 270.

[14] R. J.-M. Cramer, *An Evaluation of Ultrawideband Propagation Channels*, Ph.D Dissertation, USC, 2000.

[15] C. Dill, "Foliage Penetration (Phase II) Field Test: Narrowband versus Wideband Foliage Penetration," *Final Report of Contract Number F41624-03-D-7001/04*, July 2005 to Feb 2006.

[16] J. G. Fleischman, et al, "Foliage penetration experiment: Part I: Foliage attenuation and backscatter analysis of SAR imagery," *IEEE Transactions on Aerospace and Electronic Systems*, vol. 32, no. 1, part 1 of 3, 134144, 1996.

[17] J. A. Hogbom, "Aperture synthesis with a non-regular distribution of interferometer baseline," *Atronomy and Astrophysics Supplement Ser.*, vol. 15, 1974.

[18] T.-C. Hou and T-J. Tsai, " An access-based clustering protocol for multihop wireless ad hoc networks," *IEEE J. Selected Areas in Communications*, vol. 19, no. 7, pp. 1201-1210, July 2001.

[19] I. Y. Immoreev, "New practical application of ultra-wideband radars," *2007 European Radar Conference, 2007*, Oct. 2007, pp. 216 - 219.

[20] A. Iwata, C. C. Chiang, G. Pei, M. Gerla, and T. W. Chen, " Scalable routing strategies for ad hoc networks," *IEEE J. Selected Areas in Communications*, vol. 17, pp. 1369-1379, 1999.

[21] R. Kapoor, et al, "UWB radar detection of targets in foliage using alpha-stable clutter models," *IEEE Trans on Aerospace and Electronic Systems*, vol. 35, no. 3, July 1999, pp. 819 - 834.

[22] B. Levitas, J. Matuzas, "UWB Radar for Human Being Detection Behind the Wall," *Proc. of 2006 Intl Radar Symposium*, May 2006, pp. 1 - 3.

[23] Q. Liang, S. Samn, X. Cheng, "UWB Radar Sensor Networks for Sense-through-Foliage Target Detection," *IEEE International Conference on Communications*, May 2008, Beijing, China.

[24] Q. Liang, et al, "Opportunistic Sensing in Wireless Sensor Networks: Theory and Applications," *IEEE Trans on Computers*, vol. 63, no. 8, pp. 2002-2010, August 2014.

[25] S. Liang, "Sense-through-wall human detection based on UWB radar sensors," *Signal Processing*, vol. 126, pp. 117-124, Sept 2016.

[26] C. R. Lin and M. Gerla, "Adaptive clustering in mobile wireless networks," *IEEE J. Selected Areas in Communications*, vol. 16, pp. 1265-1275, 1997.

[27] I. Maherin, Q. Liang, "Multi-Step Information Fusion for Target Detection using UWB Radar Sensor Network," *IEEE Sensors Journal*, vol. 15, no. 10, pp. 5927-5937, Oct 2015.

70

[28] J. W. McCorkle, "Early results from the ARL UWB Foliage Penetration (FOPEN) SAR," *SPIE International Symposium on Optical Engineering and Photonics in Aerospace and Remote Sensing, Underground and Obscured Object Detection*, Apr. 1993.

[29] C. E. Perkins, "Chapter 4, Cluster-Based Networks," *Ad Hoc Networking*, Edited by C. E. Perkins, pp. 75-138, Addison-Wesley, 2001.

[30] M. A. Richards, *Fundamentals of Radar Signal Processing*, McGraw-Hill Companies, New York, 2005.

[31] M. P. Rowe, E. N. Pugh, Jr., J. S. Tyo, and N. Engheta, "Polarization-difference imaging: a biologically inspired technique for observation through scattering media," *Optics Letters*, Vol. 20, pp. 608-610, 1995.

[32] J. Roman, M. Rangaswamy, D. Davis, Q. Zhang, B. Himed, and J. Michels, "Parametric adaptive matched filter for airborne radar applications," *IEEE Trans. Aerosp. Electron. Syst.*, vol. 36, no. 2, pp. 677-692, 2000.

[33] M. I. Skolnik, *Introduction to Radar Systems*, 3rd ed, New York, McGraw Hill, 2001.

[34] R. A. Scholtz, M. Z. Win, and J. M. Cramer, "Evaluation of the Characteristics of the ultra-wideband propagation channel," *Proc of Antenna and Propagation Symposium*, vol. 2, no. 626-630, 1998.

[35] D. R. Sheen, et al, "Foliage transsmission measurements using a ground-based ultrawideband (UWB) (3001300 Mhz) SAR system," *IEEE Transactions on Geoscience and Remote Sensing*, vol. 32, no. 1, 1994.

[36] S. Sowelam and A. Tewfik, "Waveform selection in radar target classification," *IEEE Trans on Information Theory*, vol. 46, no. 3, pp. 1014-1029, 2000.

[37] L. Stankovic, T. Thayaparan, M. Dakovic, "Signal Decomposition by Using the S-Method with Application to the Analysis of HF Radar Signals in Sea-Clutter," *IEEE Trans. on Signal Processing*, vol. 54, no. 11, pp.4332-4342, Nov. 2006.

[38] Y. Sun, P. Willett, and R. Lynch, "Waveform fusion in sonar signal processing", *IEEE Transactions on Aerospace and Electronic Systems*, Vol. 40, No. 2, 2004

[39] J. D. Taylor, *Ultra-wideband radar technology*, CRC Press, 2001.

[40] J. D. Taylor, *Introduction to Ultra-Wideband Radar Systems*, CRC Press, 1995.

[41] J. S. Tyo, M. P. Rowe, E. N. Pugh, Jr., N. Engheta, "Target detection in optically scattering media by polarization difference imaging," *Applied Optics*, Vol. 35, pp. 1855-1870, 1996.

[42] Ericsson White Paper, "Heterogeneous Networks,", Feb. 2012.

[43] M. Gudmundson, "Cell Planning in Manhattan Environments,", IEEE Vehicular Technology Conference, Spring 1992.

[44] W. Liu, et al., "Massive MIMO or small cell network: Who is more energy efficient?," IEEE Wireless Communications and Networking Conference Workshops, April 2013.

[45] Y. Wu, P. Butovitsch, M. Zhang, "Capacity Upper Bound for Adding Cells in the Super Dense Cellular Deployment Scenario," Vehicular Technology Conference, 2014

[46] Q. Wu and Q. Liang, "Increasing capacity of muti-cell cooperative cellular networks with nested deployment," IEEE International Conference on Communications, June 2015

[47] P. Pal and P.P. Vaidyanathan,"Theory of Sparse Coprime Sensing in Multiple Dimensions," IEEE Trans. on Signal Processing, vol. 59, no. 9, pp. 3592-3608, Aug. 2011

[48] A.D. Wyner, "Shannon-theoretic approach to a Gaussian cellular multipleaccess channel," *IEEE Trans. Information Theory*, vo1. 40, no. 6, pp. 1713-1727, Nov. 1994.

[49] O. Somekh, B.M. Zaidel, and S. Shamai, "Sum rate characterization of joint multiple cell-site processing," IEEE Trans. Information Theory, vol. 53, no. 12, pp. 4473-4497, Dec. 2007.

[50] M. I. Skolnik, "Introduction to Radar System", 3rd ed, New York, McGraw Hill, 2001.

[51] P. Pal and P. P. Vaidyanathan, "Nested arrays: a novel approach to array processing with enhanced degree of freedom," *IEEE Trans. Signal Process*, pp. 4167-4181, Aug. 2010.

[52] P. Pal, and P. P. Vaidyanathan, "Sparce sensing with co-prime samplers and arrays," *IEEE Trans. Signal Process*, Vol. 59.2, pp. 773-586, 2011.

[53] P. Pal, and P. P. Vaidyanathan, "Nested arrays in two dimensions, part II: application in two dimensional array processing," *IEEE Trans. Signal Process*, Vol. 60.9, pp. 4706-4718, 2012.

[54] P. Piya, and P. P. Vaidyanathan, "Nested arrays in two dimensions, part I: geometrical consideration," *IEEE Trans. Signal Process*, Vol. 60.9, pp. 4694-4705, 2012.

[55] A. Moffet, "Minimum-redundancy linear arrays," *IEEE Transaction*, Vol. 16.2, pp 172-175, 1968.

[56] S. M. Luria, J. A. S. Kinney, S. Weissman, "Estimation of size and distance underwarer," *The American Journal of Psychology*, Vol. 80, pp. 282-286, Jun. 1967.

[57] Q. Liang, and X. Cheng, "KUPS: Knowledge-based ubiquitous and persistent sensor networks for threat assessment," *IEEE Trans. AAES*, Vol. 44.3, pp. 1060-1069, 2008.

[58] S. Petre, and N. Arye, "MUSIC, maximum likelihood, and Cramer-Rao bound: further results and comparisons," *IEEE Trans. ASSP*, Vol.38.12, pp. 2140-2150, 1990

[59] P. P. Vaidyanathan, "Multirate Systems and Filter Banks. Englewood Cliffs", NJ: Prentice-Hall, 1992

[60] V. Venkatasubramanian and Henry Leung, "A Novel Chaos-Based High-Resolution Imaging Technique and Its Application to Through-the-Wall Imaging," *IEEE Signal Proc Letters*, Vol. 12, No. 7, July 2005.

[61] P. Withington , H. Fluhler, and S. Nag , "Enhancing homeland security with advanced UWB sensors," *IEEE Microwave Magazine*, Sept 2003.

[62] A. G. Yarovoy, et. al, "UWB Radar for Human Being Detection," *IEEE Aerospace and Electronic Systems Magazine*, vol. 23, no. 5, May 2008, pp. 36 - 40.

[63] D. K. Barton, *Radar System Analysis and Modeling*, Artech House, Boston, MA, 2006.

[64] C. Bruce C, R. Desimone, C. G. Gross, "Visual properties of neurons in a polysensory area in superior temporal sulcus of the macaque," *J. Neurophysiol.*, vol. 46 369 84, 1981.

[65] D. A. Chavis, D. N. Pandya, "Further observations on cortico-frontal connections in the rhesus monkey," *Brain Res.*, vol. 117, pp. 369386, 1976.

[66] B. A. Dosher, G. Sperling, and S. A. Wurst, "Tradeoffs between stereopsis and proximity luminance covariance as determinants of perceived 3D structure," *Vision Research*, vol. 26, No. 6, pp. 973-990, 1986.

[67] N. V. S. Graham, "Visual pattern analyzers," pp. xvi, 646, New York, NY, US: Oxford University Press, 1989.

[68] J. M. Hillis, M. O. Ernst, M. S. Banks, and M. S. Landy, "Combining sensory information: Mandatory fusion within, but not between, senses," *Science*, vol. 298, No. 5598, pp. 1627-1630, 2002.

[69] T.-C. Hou and T-J. Tsai, " An access-based clustering protocol for multihop wireless ad hoc networks," *IEEE J. Selected Areas in Communications*, vol. 19, no. 7, pp. 1201-1210, July 2001.

[70] A. Iwata, C. C. Chiang, G. Pei, M. Gerla, and T. W. Chen, " Scalable routing strategies for ad hoc networks," *IEEE J. Selected Areas in Communications*, vol. 17, pp. 1369-1379, 1999.

[71] E. G. Jones, T. P. S. Powell, An anatomical study of converging sensory pathways within the cerebral cortex of the monkey," *Brain*, vol. 93, pp. 793-820, 1970.

[72] Q. Liang, "Biologically-Inspired Target Recognition in Radar Sensor Networks," *International Conference on Wireless Algorithms, Systems, and Applications*, August 2009, Boston, MA.

[73] C. R. Lin and M. Gerla, "Adaptive clustering in mobile wireless networks," *IEEE J. Selected Areas in Communications*, vol. 16, pp. 1265-1275, 1997.

[74] J. M. Mendel, *Uncertain Rule-Based Fuzzy Logic Systems*, Prentice-Hall, Upper Saddle River, NJ, 2001.

[75] E. K. Miller, "The prefrontal cortex: complex neural properties for complex behavior," *Neuron*, vol. 22, pp. 1517, 1999.

[76] E. K. Miller, J. D. Cohen, "An Integrative Theory of Prefrontal cortex function," *Annu. Rev. Neurosci.*, vol. 24, pp. 167, 2001.

[77] ONR BAA 07-017, "NET-SENTRIC Surveillance," http://www.onr.navy.mil/02/baa/.

[78] R. C. OReilly, "Biologically Based Computational Models of High-Level Cognition," *Science*, Oct 2006.

[79] D. N. Pandya, C. Barnes, "Architecture and connections of the frontal lobe," *The Frontal Lobes Revisited*, ed. E Perecman, pp. 41 72. New York: IRBN, 1987.

[80] D. G. Pelli, "Uncertainty explains many aspects of visual contrast detection and discrimination," *Journal of the Optical Society of America*, vol. A, No. 2, pp. 1508-1532, 1985.

[81] I. I. Immoreev, P.G.S.D.V. Fedotov, *"Ultra wideband radar systems: advantages and disadvantages,"*IEEE Conference on Ultra Wideband Systems and Technologies, .pp.201-205, 2002.

[82] S. I. Dimitriadis, Y. Sun, K. Kwok, N. A. Laskaris, N. Thakor, A. Bezerianos, *"Revealing cross-frequency causal interactions during a mental arithmetic task through symbolic transfer entropy: a novel vector-quantization approach"* in IEEE Trans Neural Syst Rehabil Eng., Epub ahead of print, Jan 2016.

[83] C. Yang, R. Le Bouquin Jeannes, J. Bellanger, H. Shu, *"A new strategy for model order identification and its application to transfer entropy for EEG signals analysis"*, IEEE Trans. Biomed. Eng., vol. 60, no. 5, pp. 1318-1327, May 2013.

[84] X. Bian, Y. Shao, H. Gong, F. Zhang and C. Xie, *"Subsurface targets detection with Shannon entropy"*, Geoscience and Remote Sensing Symposium, 2011 IEEE international, Oct. 2011.

[85] J. Shigong, K. Lingjiang, *"A new approach to range spread target detection based on information entropy"*, 2nd Asian-Pacific Conference on Synthetic Aperture Radar, APSAR 2009., pp.560-562, 26-30 Oct. 2009.

[86] Y. Yu, C. Chen, X. Feng and C. Liu, *"Application of entropy classification method to the detection of subsurface linnear targets in polarimetric GPR data"*, Geoscience and Remote Sensing Symposium, IEEE international, Nov. 2016.

[87] X. Wang, J. Liu, H. Liu, *"Small Target Detection in Sea Clutter Based on Doppler Spectrum Features,"* International Conference on Radar,. CIE '06., pp.1-4, 16-19 Oct. 2006.

[88] I. Maherin and Q. liang, *"A mutual information based approach for target detection through foliage using UWB radar,"* Workshop on Radar and Sonar Network, pp. 6406-6410, 2012.

[89] A. Kaiser, T. Schreiber, *"Information transfer in continuous processes"*, Physica D Vol. 166, Issues1-2, June, 2002.

[90] C.Dill, *"Foliage Penetration(phase II) Field Test Narrow band vesus Wideband Foliage Penetration,"* Final report of contract number F41624-03-D-700/04, July 2005 to Feb 2006.

[91] Q. Liang, et al, *"Opportunistic Sensing in Wireless Sensor Networks: Theory and Applica- tions,"* IEEE Trans on Computers, vol. 63, no. 8, pp. 2002-2010, August 2014.

[92] I. Maherin, Q. Liang, *"Multi-Step Information Fusion for Target Detection using UWB Radar Sensor Network,"* IEEE Sensors Journal, vol. 15, no. 10, pp. 5927-5937, Oct 2015.

[93] S. Liang, *"Sense-through-wall human detection based on UWB radar sensors,"* Signal Process- ing, vol. 126, pp. 117-124, Sept 2016.

[94] Y. Lu and E. Sang, *"Underwater target size/shape dynamic analysis for fast target recognition using sonar images,"* 1998 International Symposium on Underwater Technology, pp. 172-175, 1998.

[95] Q. Liang and X. Cheng, *"Underwater Acoustic Sensor Networks: Target Size Detection and Performance Analysis,"* Ad Hoc Networks Journal (Elsevier), vol. 7, no. 4, pp. 803-808, June 2009,

[96] C. E. Perkins, "Chapter 4, Cluster-Based Networks," *Ad Hoc Networking*, Edited by C. E. Perkins, pp. 75-138, Addison-Wesley, 2001.

[97] P. Withington , H. Fluhler, and S. Nag , "Enhancing homeland security with advanced UWB sensors," *IEEE Microwave Magazine*, Sept 2003.

[98] K. M. Yemelyanov, J. A. McVay, N. Engheta, A. Hoorfar, "Adaptive Polarization-Difference Imaging Algorithms for Through-the-Wall Microwave Imaging Scenarios," *Proc. IEEE AP-S Int. Symposium and USNC/URSI National Radio Science Meeting*, July 3-6, 2005, Washington DC, USA.

BIOGRAPHICAL STATEMENT

Hao Liang was born in Tianjin, China in 1989. He received his B.S. degree from Case Western Reserve University, USA, in 2013, his Ph.D. degrees from The University of Texas at Arlington in 2017, respectively, all in Electrical Engineering. His research interests include wireless communications, target detection and statistical signal processing.